Changes in mean and extreme precipitation scale universally with global mean temperature across and within climate models

Maximilian Kotz[a b] , Stefan Lange [a] , Leonie Wenz [a c] , Anders Levermann [a b d]

[a] *Potsdam Institute for Climate Impact Research*

[b] *Innstitute of Physics, University of Potsdam*

[c] *Mercator Research Institute on Global Commons and Climate Change*

[d] *Lamont-Doherty Earth Observatory, Columbia University*

Note this is a non peer-reviewed preprint submitted to EarthArXiv.
The manuscript has been submitted to Journal of Climate.
Twitter: @KotzMaximilian

Corresponding author: Maximilian Kotz, maxkotz@pik-potsdam.de

ABSTRACT: Projections of precipitation from global climate models are crucial for risk assessment and adaptation strategies under different emission scenarios, yet model uncertainty limits their application. Here, we assess inter-model differences by separating the response of precipitation to anthropogenic forcing within 21 individual, bias-adjusted CMIP6 models using a pattern filtering technique. The forced response of mean precipitation, the number of wet days and the intensity and frequency of daily extremes are identified using low-frequency component analysis. Inter-model agreement in the sign of local change is moderate across land areas, with better agreement for extreme metrics (90% of models agree on 51, 41, 61, 61% of land area, for each metric respectively). Differences in the average magnitude of local changes are also large but can be explained well by the magnitude of global surface warming, despite model differences in the sign of local change (R^2 of 0.81, 0.79, 0.69, 0.79). Moreover, we show that these temperature-precipitation scaling relationships can be identified robustly within individual climate models from inter-temporal changes in the detected forced response (median R^2 of 0.82, 0.82, 0.76, 0.87). Inter-model spread in these relationships is considerable (coefficient of variation of 22, 33, 26, 17%), thus diagnosing a source of the uncertainty in the magnitude of projected precipitation change. These results suggest that despite uncertainty in the sign of regional change, the magnitude of future precipitation changes is well constrained by temperature-scaling relationships both across and within models. They may offer a new avenue to constrain the magnitude of future projections.

1. Introduction

The hydrological cycle is likely to account for a considerable portion of the impacts of future climate change. Key aspects of social well-being, such as agricultural productivity (Liang et al. (2017)), flood damages (Davenport et al. (2021); Willner et al. (2018b)), social stability (Hsiang et al. (2013); von Uexkull et al. (2016)), and economic growth (Damania et al. (2020); Holtermann (2020); Kotz et al. (2022)) are closely linked to changes in precipitation. Climate models such as those in the Coupled Model Intercomparison Project (CMIP6; Eyring et al. (2016)) play a crucial role in providing projections of precipitation under different levels of greenhouse forcing at the regional and temporal detail necessary for assessment of these impacts (Warszawski et al. (2014)). These assessments are subsequently critical in informing policy decisions regarding both mitigation (Lange et al. (2020); Thiery et al. (2021)) and adaptation (Willner et al. (2018a); Boulange et al. (2021)). Given their crucial role in this process, a thorough understanding of CMIP projections is necessary, in particular of the extent and causes of inter-model discrepancies.

Components of precipitation change in response to greenhouse forcing can be broadly characterised as thermodynamic and dynamic (Emori and Brown (2005); Seager et al. (2010); Marvel and Bonfils (2013)), resulting from either the Clausius-Clapeyron relation between atmospheric temperature and water vapor content or from shifting atmospheric currents. The interplay of these mechanisms often determines the nature of projected changes for different precipitation characteristics, as well as the extent of inter-model uncertainty. For example, the intensity of daily precipitation extremes have undergone a near-global increase (Min et al. (2011); Zhang et al. (2013); Fischer and Knutti (2016); Chen and Sun (2017); Kirchmeier-Young and Zhang (2020); Madakumbura et al. (2021)) dominated by a thermodynamic contribution with small inter-model discrepancy (Pfahl et al. (2017)). Dynamical changes from atmospheric circulation cause only regional differences in the magnitude of these increases, but contribute the majority of the uncertainty between models (Pfahl et al. (2017)).

For seasonal and annual averages, thermodynamic processes are expected to lead to a "rich-get-richer" effect in which historical differences in regional precipitation are intensified (Seager et al. (2010); Marvel and Bonfils (2013)). However, across the tropics a weakening of the tropical circulation counteracts this effect (Vecchi and Soden (2007); Seager et al. (2010); Chadwick et al. (2013)) and the pattern of mean precipitation change is therefore largely determined by shifting atmospheric currents with large inter-model uncertainty (Chadwick et al. (2013); Ma and Xie (2013); Kent et al. (2015); Long et al. (2016)). Atmospheric dynamics have also been diagnosed as a prominent source of uncertainty in projections of mean precipitation in extra-tropical regions (Shepherd (2014); Fereday et al. (2018)). In general, changes to seasonal and annual averages are projected to be heterogeneous with large inter-model uncertainty, often even in the sign of regional change (Chadwick et al. (2016)).

With the aim of better constraining precipitation projections, we here provide an assessment of future changes across 21 bias-adjusted (Lange (2019, 2021)) members of the CMIP-6 ensemble. To assess characteristics of the distribution of precipitation with relevance to societal outcomes (Kotz et al. (2022)), we separately assess mean precipitation, the number of wet days, and the frequency and intensity of daily extremes (see Methods). We use a pattern-filtering technique (Wills et al. (2018)) to separate the time-varying response to anthropogenic forcing from internal variability within each model, allowing an assessment of individual model biases in the response of each precipitation characteristic. We find that despite large differences in the spatial pattern and sign of regional change, the average magnitude of local changes scales strongly with global mean 2-m temperature (GMT) change, both across and within models. This suggests that even when dynamic processes dominate, resulting in regionally heterogeneous changes with large inter-model uncertainty, the intensity of these changes can be related back to the underlying thermodynamic driver. These clear relations may help inform probabilistic assessments of the magnitude of regional precipitation change (Chadwick et al. (2016)), valuable while the dynamical atmospheric response and the resulting signs of regional change remain uncertain (Shepherd (2014)). Moreover, the identification of precipitation-temperature scaling relationships for individual climate models could be used to constrain multi-model projections by comparison to the relationships observed in the historical record.

2. Data and Methods

a. Bias-adjusted CMIP6 data

We use daily surface precipitation rates and daily 2-m temperature from 21 climate models participating in CMIP6. We choose models which provide output under both the historical (1850-2014) and the future (2015-2100) greenhouse forcing scenarios specified by SSP126 and SSP585.

Models are bias-adjusted and statistically down scaled to a common half-degree grid to reflect the historical distribution of daily precipitation and temperature using the trend-preserving method developed in the Inter-Sectoral Impact Model Intercomparison Project (ISIMIP) (Lange (2019, 2021); Cucchi et al. (2020); Lange et al. (2021)).

b. Precipitation indices

To assess characteristics of the distribution of daily precipitation with relevance to societal outcomes (Kotz et al. (2022)), we calculate four annual precipitation indices over land-areas at the grid-cell level: the annual mean precipitation (calculated over all days), the annual number of wet days, the annual daily maximum (Rx1) as a measure of the intensity of daily extremes, and the annual number of days exceeding the 99^{th} percentile of the historical distribution (R>99p, historical percentiles calculated over all days from 1850-1950) as a measure of the frequency of daily extremes.

c. Separating the forced response from internal variability: low-frequency component analysis

Identifying the forced response of the climate system to anthropogenic influence is complicated by natural internal variability (Deser et al. (2012)), particularly on the multi-decadal time-scales over which averages are often used to characterise a forced response (Masson-Delmotte et al. (2021)). One approach to overcome this issue is to use large ensembles of a single climate model in which internal variability can be characterised and removed by initialising ensemble members from different initial conditions (Kay et al. (2015)). However, to consider the full range of structural model differences which can bias the forced response, a variety of climate models must be assessed. We do so using the multi-model ensemble CMIP6, and instead apply a pattern filtering technique to individual ensemble members to separate the forced response from internal variability. Low-frequency component analysis (LFCA) takes advantage of the different time-scales of the respective processes to identify the forced response to anthropogenic influence with accuracy comparable to single-model ensembles with up to 20 members (Wills et al. (2020)).

Here we provide a conceptual summary of LFCA and of its application to identifying the climatic response to anthropogenic forcing, please see Wills et al. (2018) for a more detailed introduction to and description of the method. LFCA is a form of linear-discriminant analysis which identifies independent modes which can account for the greatest ratio of low-frequency to total variance. Given the longer time-scales over which changes due to greenhouse forcing evolve in comparison to those due to internal variability, this form of variance maximisation can accurately separate the two (Wills et al. (2018, 2020); Kotz et al. (2021)). Linear recombinations of the leading empirical-orthogonal-functions (EOFs) are found which maximise this variance ratio. We retain a sufficient number of EOFs to account for a minimum of 70% of the spatio-temporal variance, and define low-frequency variance as that following filtering with a 20-year low-pass Butterworth filter with reflecting boundary conditions. We use a lower cut-off frequency than Wills et al. (2018, 2020), due to the lower signal-to-noise ratio of the climate change signal in precipitation than temperature (Deser et al. (2014)), but recover consistent results under alternative filtering specifications. The resulting linear recombinations are independent, and ordered in terms of increasing frequency. They constitute both a "low-frequency component" (LFC) and "low-frequency pattern" (LFP); the LFC is a time-series which describes the temporal evolution of the specific spatial pattern encompassed by the LFP. We interpret the lowest-frequency component as the response to anthropogenic forcing, following Wills et al. (2020) and Kotz et al. (2021).

We apply low-frequency component analysis to the four precipitation indices and to annual mean temperature from 1950-2100 under the anthropogenic forcing of the historical period and both the SSP126 and SSP585 future scenarios, having first linearly interpolated to a 1-by-1 degree grid due to computational constraints. The forced change between two given time periods (usually between two decades) is then calculated as the product of the lowest-frequency LFP and the difference between temporal (usually decadal) averages of the corresponding LFC.

3. Results

a. The precipitation response to anthropogenic-forcing in individual climate models

We identify the response of mean daily precipitation, the number of wet days and the intensity and frequency of daily extremes to anthropogenic forcing (historical and SSP585) within individual CMIP6 climate models using low-frequency component analysis, the results of which are shown in Figs. 1 to 4 (for results under historical and SSP126 forcing see Figs. A1-4). For each precipitation index and for each model, the lowest-frequency component (LFC-1) exhibits a near-monotonic trend which closely follows the increasing concentrations of greenhouse gases in the historical and SSP585 scenario. In Figs. 1 to 4 we show LFC-1 for each model overlain in comparison to the time-series of greenhouse gas concentrations. However, both the intensity and spatial pattern of the detected end-of-century forced change (1950-60 to 2090-2100) show clearer differences between models. Maps of the forced-change are displayed separately for each model to present the full heterogeneity of modelling bias. Moreover, by ordering models in terms of their GMT change (the area-weighted global average of the end-of-century forced change in annual mean 2-m temperature, estimated with LFCA), a dependence of the intensity of forced precipitation change on GMT change becomes visible. This dependence is explored more thoroughly in Section 3.c.

b. The spatial patterns of forced change - intermodel uncertainty

The spatial patterns of forced change in mean precipitation (Fig. 1) are similar to that identified by Masson-Delmotte et al. (2021), particularly in the ensemble mean (Fig. 5a). Increases across most of the global land mass contrast decreases across the Mediterranean basin, Central America, and the southern tips of South America, Africa and Australia. We find the response of the number of wet days (Figs. 2, 5b) to follow this pattern closely (see Fig. B1 for an explicit assessment) but with generally smaller increases and more wide-spread regional reductions. This difference may arise due to the expected shift to fewer light precipitation events under greenhouse forcing (Fischer and Knutti (2016)). As anticipated, the extreme indices exhibit spatial patterns with more homogeneous increases (Figs. 3, 4, 5c-d), although regional reductions are found, often corresponding to regions of large mean precipitation reduction (see Figs. B2 and B3). In the ensemble means (Figs. 5c-d), these regions (the Mediterranean Basin and Southern tip of Africa and South America) match those identified by Pfahl et al. (2017) as having large dynamical contributions which oppose the general thermodynamic increases in extreme precipitation. Increases in the frequency of daily extremes are particularly large, exceeding 200% in large regions of a number of models (Fig. 4), confirming the importance of assessing both the frequency and intensity of extremes for impact assessments (Myhre et al. (2019)).

Fig. 5 shows the ensemble mean change for each precipitation index, with regions stippled where less than 80% of models agree on the sign of change. Disagreement between models is often concentrated at the boundary between regional increases and decreases, likely where uncertainty in the dynamic atmospheric response is large (Kent et al. (2015)). In the case of the extreme indices, this constitutes the Mediterranean basin, central America, southern Africa, central South America and Australia. The patterns of disagreement are similar for the other two indices, but are generally more widespread, particularly across North America, South-East Asia, and particularly for the number of wet days. We assess the extent of inter-model agreement in the spatial patterns of change using two metrics. Fig. 6a shows the percentage of land area on which models agree on the sign of change, as a function of the number of models in agreement. This metric shows best agreement for the extreme indices, for which 90% of models agree on approximately 61% of the land area. By comparison, 90% of models agree on only 51% and 41% of land area for the mean precipitation and the number of wet days respectively. Alternatively, we calculate centred pattern correlations (Santer et al. (1995)) between the forced changes of each index in unique pairs of climate models, shown in Fig. 6b. This is likely to capture differences in the relative magnitude of regional changes in addition to the sign of change. The frequency of daily extremes still shows the best inter-model agreement (median correlations of 0.70), but mean precipitation changes show similarly high values (median correlations of 0.69). Agreement in the number of wet days and in the intensity of daily extremes are lower (median correlations of 0.65 and 0.53).

Moreover, we briefly test the benefits of identifying the forced response using LFCA in comparison to standard temporal averages. Pattern correlations between models are significantly higher when precipitation changes are calculated after detection with LFCA (Fig. B4). Improvements are particularly large in the SSP126 scenario in which the climate change signal-to-noise ratio is smaller compared to SSP585 (see the percentage of total spatio-temporal variance explained by the lowest-frequency component in SSP585 vs SSP126 in Figs. 1-4 and A1-A4). This suggests that LFCA most considerably improves the detection of the forced response in the context of large internal variability relative to the magnitude of forced climate change.

c. The magnitude of forced change - temperature-precipitation scaling across models

Given the considerable inter-model uncertainty in the projected sign of regional precipitation change, particularly for the mean and the number of wet days, an assessment of the magnitude of future changes which implicitly accounts for these uncertainties may be helpful. For example, although differing shifts in atmospheric currents may lead to inter-model uncertainty in the sign of regional precipitation change (Chadwick et al. (2014); Kent et al. (2015)), the magnitude of such changes may be more consistent between models (Chadwick et al. (2016)). We consider the land-averaged (excluding Antarctica) absolute percentage change as an indicator of the magnitude of change which is independent of the specific signs of regional change. By taking percentages before spatial averaging we focus on the magnitude of local change, arguably with most relevance from an impact perspective.

For each precipitation index, this metric varies considerably across models within a given forcing scenario but can be explained well by the extent of GMT change, Fig 7. Fitting exponential regressions to these changes accounts for a considerable amount of the variance across models and scenarios (81, 79, 69 and 79%, for each metric respectively). For comparison, we conduct a similar analysis without having taken absolute values, in which a smaller portion of precipitation change can be explained by GMT (66, 48, 66 and 75%, for each metric respectively), particularly for mean precipitation and the number of wet days (Fig. C1). This improvement when taking absolute values suggests that when shifting atmospheric currents contribute large uncertainty to the sign of regional precipitation change, the intensity of these dynamic changes can still be closely related to the underlying thermodynamic driver (see further discussion in section 4). Moreover, we also conduct a similar assessment taking percentage changes at the global rather than local level, (Figure C2), replicating the known scaling between net global precipitation and GMT change of approximately $2\%K^{-1}$ (Stephens and Ellis (2008)).

As a further conceptual analysis, we compare these temperature-precipitation scaling relationships to those anticipated due solely to the theoretical thermodynamic contribution of the Clausius-Clapeyron (CC) relation between water-vapour content and temperature. For mean precipitation and the intensity of daily extremes (Rx1) this should follow the near-surface water vapour scaling of $6.1\%\mathrm{K}^{-1}$ (Bao et al. (2017)). The identified CMIP6 scalings are close to but slightly below this relation, at $5.7\%\mathrm{K}^{-1}$ and $5.3\%\mathrm{K}^{-1}$ respectively.

For the number of wet days and the frequency of daily extremes, we follow Fischer and Knutti (2016) to estimate a theoretical thermodynamic scaling. We apply the CC relation for a given GMT change to each day of the historical precipitation distribution (1850-1950) and then re-calculate the indices on the re-scaled distribution. For the frequency of daily extremes (R>99p), the scaling expected from the CC relation is considerably higher than for the mean and intensity of extremes,

$14.8\%K^{-1}$. The scaling identified within CMIP6 also shows higher values but falls short of the CC relation at $10.3\%K^{-1}$. By contrast, the CC relation predicts a much weaker scaling of $1.8\%K^{-1}$ for the number of wet days. The observed CMIP6 scaling is also weaker for this index compared to the others, but in this case is considerably larger than the theoretical scaling, $4\%K^{-1}$. Moreover, we find that the observed CMIP6 scalings match more closely the theoretical CC relation when using GMT rather than land mean 2-m temperature change (compare to Fig. C3), intuitive given the dominant oceanic source of moisture for continental precipitation.

These theoretical expectations explicitly ignore dynamical contributions to precipitation change from shifting atmospheric currents, and more complex relationships between water-vapour content and precipitation rate and onset (Neelin et al. (2017)). It is interesting therefore that they provide a reasonable guide to the magnitude of scaling identified in the models. However, if thermodynamics control the net atmospheric moisture content, whereas atmospheric dynamics provide only regional redistribution of this moisture, then the application of these scalings at the global level may actually be reasonable. If moisture convergence in one region is balanced by divergence in another, then these effects would cancel out in a global average and the dominant global scaling would be determined by the thermodynamic process. The CC relation is most inaccurate for the number of wet days, likely due to the greater importance to this variable of changes to the more nuanced processes determining rainfall onset (Neelin et al. (2017)).

d. Temperature-precipitation scaling within individual models

There is considerable variance left unexplained in the scaling between forced temperature and precipitation changes across models and scenarios, suggesting that precipitation changes may scale with temperature at different rates in individual models. We test this hypothesis by assessing changes in the time-varying forced response of precipitation and temperature occurring over 25 year periods within individual climate models (identified with LFCA). This method reveals robust temperature-precipitation scaling relationships for each climate model which can explain a large proportion of the inter-temporal changes in precipitation, Figs. 8-11. When ordered in terms of GMT change, one sees that this scaling generally explains a greater proportion of variance in models with a larger GMT change, essentially due to the size of the climate change signal (see also Fig. D1).

On average, the rates at which precipitation scales with temperature change within individual models is consistent with that identified between models. However, there is considerable inter-model heterogeneity in these rates, the distribution of which is shown in Fig. 12. EC-Earth appears to be a consistent outlier, for mean precipitation and the intensity and frequency of daily extremes in particular. Excluding this model, we calculate coefficients of variation of 17-33% for these distributions, demonstrating that large inter-model uncertainty exists in the modelled rate at which precipitation changes scale with temperature. These inter-model differences in intra-model scaling rates are significant at the 10% level given our methodological uncertainty (estimated using 1000 bootstrapped replacements of inter-temporal changes) for between 47 and 64% of unique model pairs, see Fig. D2.

We find weak evidence that these differences in the scaling rate may depend on the equilibrium climate sensitivity (Fig. D3). There is, however, clear evidence for co-varying scaling rates across models between the mean precipitation and the number of wet days, and between the frequency and intensity of daily extremes, suggesting that common physical drivers underlie the model biases in these indices (Fig. D4). Weaker evidence for co-varying rates between mean precipitation and the daily extremes is also noted (Fig. D4).

4. Discussion

Here, we have applied LFCA to detect the transient response of multiple aspects of continental precipitation to anthropogenic forcing in individual CMIP6 climate models. There are large inter-model differences in the sign of local precipitation change, particularly for mean precipitation and the number of wet days (90% of models agree on only 51 and 41% of the global land mass), likely due to the uncertain contributions of shifting atmospheric currents (Kent et al. (2015)). However, we demonstrate that despite these differences, the average magnitude of local precipitation change scales strongly with GMT change across models (5.7, 4.0, 5.3 and 10.3$\%K^{-1}$ for mean precipitation, the number of wet days and the intensity and frequency of daily extremes, respectively). These results relate closely to that of Chadwick et al. (2016), but demonstrate precipitation-GMT scalings for the magnitude rather than extent of change, and across the global land mass rather than the tropics. Moreover, they complement previous understanding of the scaling between net continental precipitation and GMT change ($2\% K^{-1}$, (Stephens and Ellis (2008))), by focusing instead on the average magnitude of local precipitation change.

That a better scaling is identified when taking the absolute value of local change suggests that even when the dynamic response of the atmospheric circulation dominates precipitation change and its uncertainty, the intensity of these changes can be clearly related back to the thermodynamic driver. This is particularly clear for mean precipitation and the number of wet days, for which the dynamical response is more dominant and the improvements larger when taking absolute values. The implied importance of the thermodynamic driver for the intensity of the dynamic response is intuitive given the strong dependence of shifting atmospheric circulation on changes to sea surface temperature and land-sea temperature-gradients (Deser and Phillips (2009); Chadwick et al. (2013, 2014); Ma and Xie (2013)). Moreover, it suggests a dominant role for these thermodynamically-mediated mechanisms of circulation change in comparison to those arising directly from CO2 radiative forcing (Bony et al. (2013); Shaw and Voigt (2015); Ceppi et al. (2018)). Further research which is beyond the scope of this work would be required to explicitly evaluate the roles of these mechanisms for precipitation change.

Furthermore, we demonstrate that these scaling-relations are robustly identifiable within individual climate models, by assessing inter-temporal changes in temperature and precipitation. There are clear biases between models in the rates of this scaling, thus diagnosing a source of the uncertainty in the magnitude of precipitation projections, one worth considering in future model development.

Identification of these scaling-relations, in-spite of the large uncertainties in the sign of local change, considerably improves the utility of the CMIP6 precipitation projections. Biases in the modelling of the atmospheric response to forcing may persist for some time (Shepherd (2014)), and consequently so too will uncertainties in the sign of local change. While these remain, the here-identified temperature-precipitation relationships may help inform policy-relevant assessments by constraining the average magnitude of regional change under a given forcing scenario. On the one hand, the inter-model relationships (Fig. 7) may constrain projections when combined with best-estimates of the equilibrium climate sensitivity (Sherwood et al. (2020)). On the other hand, intra-model relationships (Figs. 8-11) may offer an opportunity to constrain ensemble projections by selecting models whose scaling better reflects those identified from the observational record. A recent assessment of changes in the frequency of extreme precipitation across Europe suggests that models in CMIP-5 strongly under-estimate observed changes for a given level of warming (Myhre et al. (2019)). If few models can accurately reproduce the observed scaling then there may be justification for even correcting model projections on the basis of observations, as for example in O'Gorman (2012).

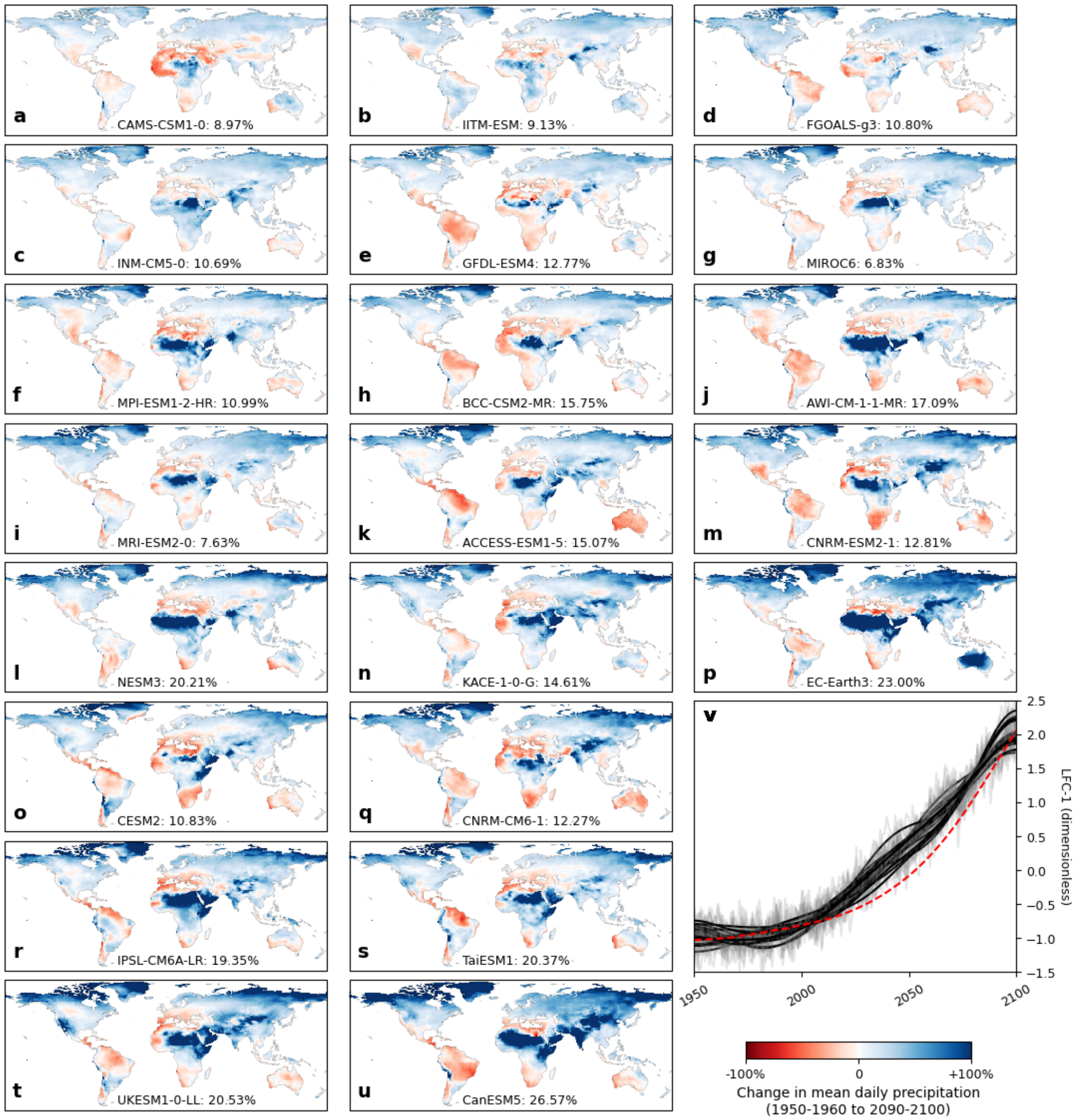

Fig. 1. The forced response of mean daily precipitation to historical (1950-2014) and future (SSP585, 2015-2100) anthropogenic forcing, detected in individual CMIP6 climate models with low-frequency component analysis. (a-u) The spatial pattern of the forced change from 1950-60 to 2090-2100 (the product of the lowest-frequency pattern with the difference between decadal averages of its corresponding component), expressed as a percentage of the historical climatology (1850-1950). Models are ordered (a-u and top-left to bottom-right) from lowest to highest projected global mean temperature increase. (v) The temporal evolution of the lowest-frequency components (LFC-1) are shown in grey with a 20-year Butterworth filtered time-series in black. Time series for each model are overlain due to their similarity. The concentration of greenhouse gases in the historical and SSP585 are rescaled and shown in red for comparison. The model name is indicated in the bottom of each panel, along with the percentage of total variance accounted for by LFC-1 in each model.

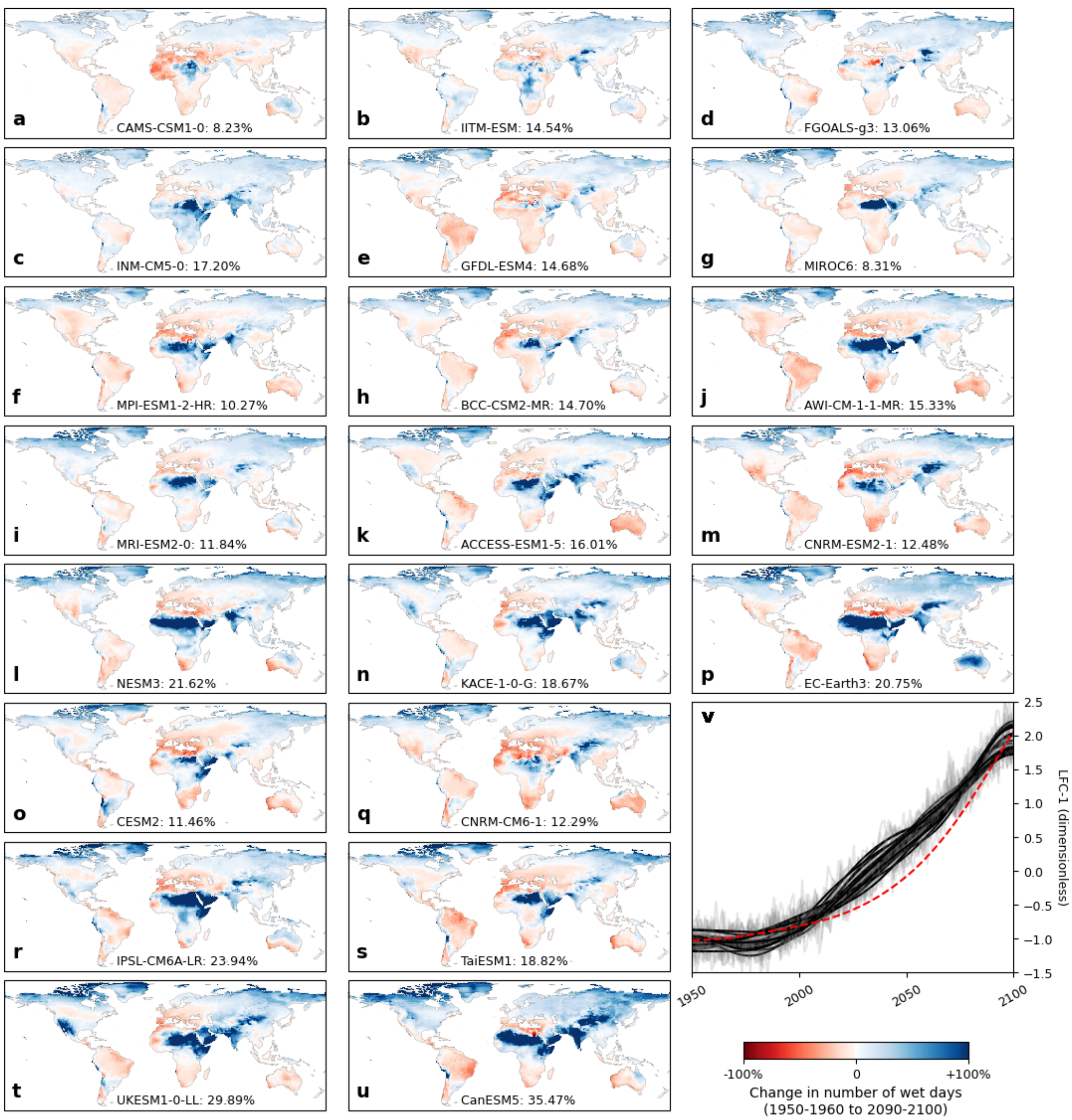

FIG. 2. The forced response of the number of wet days. As Fig. 1 but for the number of wet days.

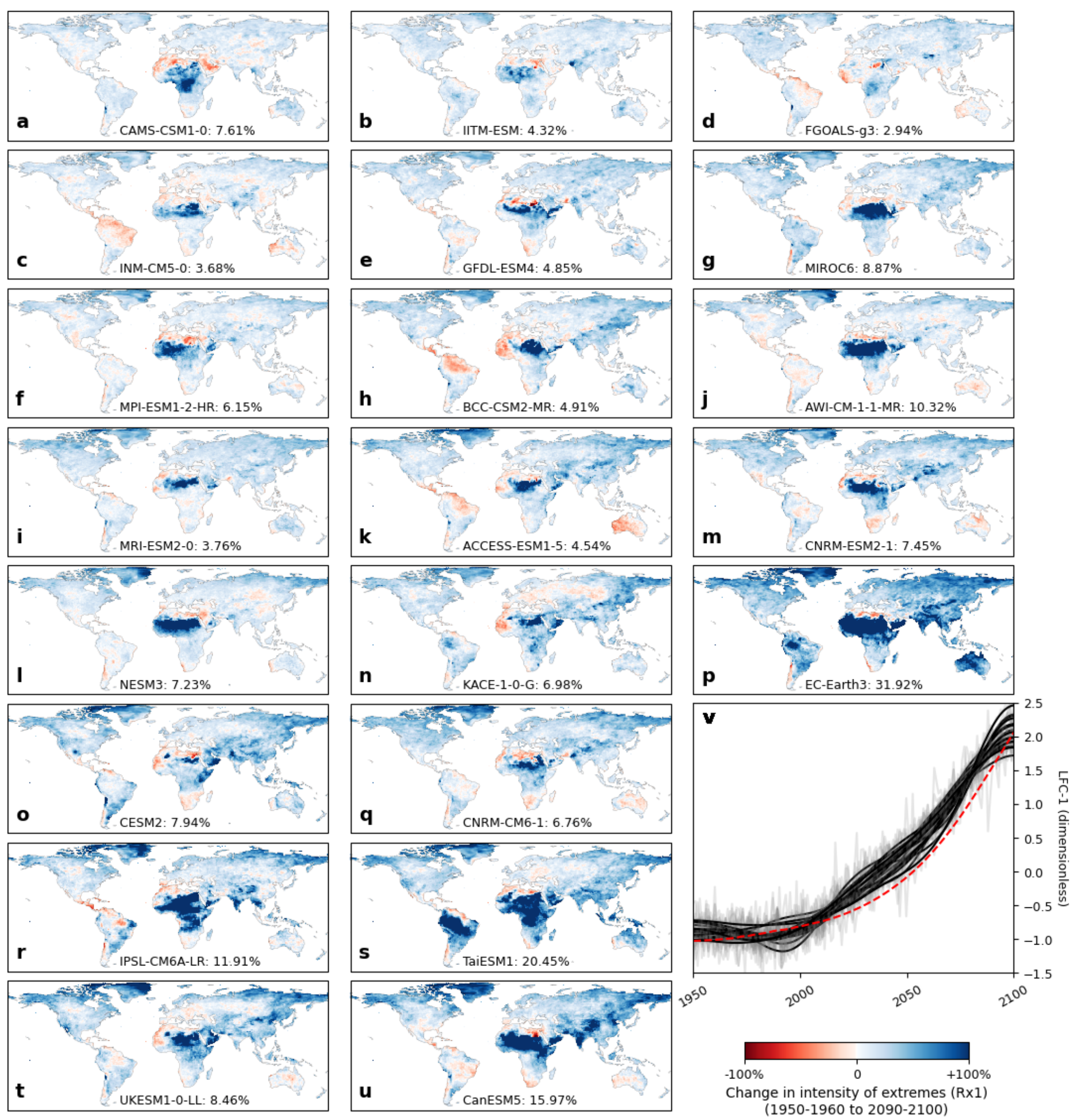

162 FIG. 3. The forced response of the intensity of daily precipitation extremes. As Fig. 1 but for the annual
163 maximum daily precipitation (Rx1).

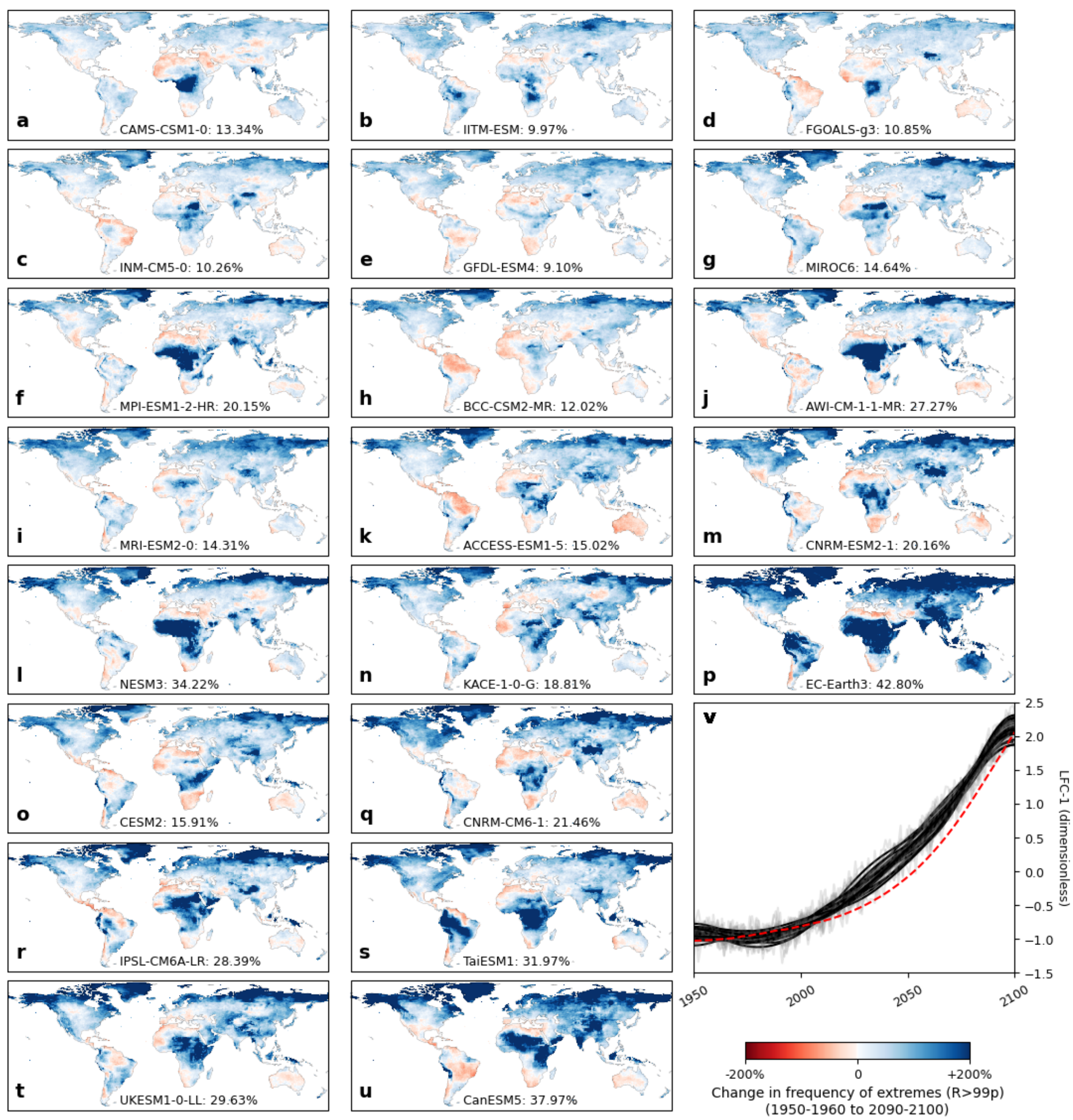

164 FIG. 4. The forced response of the frequency of daily precipitation extremes. As Fig. 1 but for the annual number of days exceeding the 99^{th} percentile of historical daily precipitation (R>99). Note the different color scale.

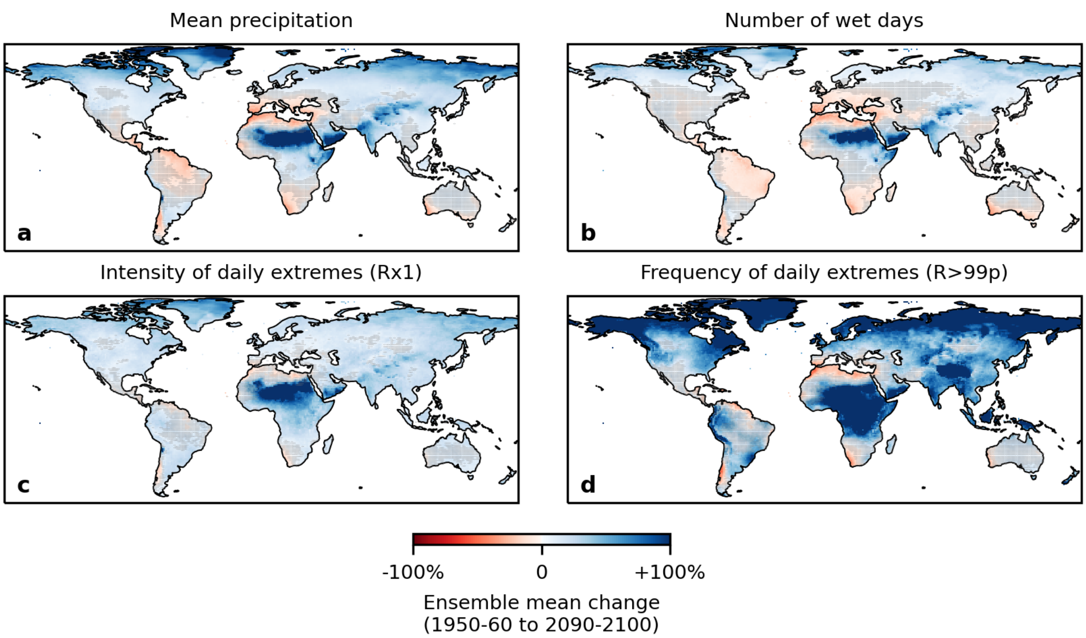

FIG. 5. The ensemble-mean forced change in mean daily precipitation (a), the number of wet days (b), and the intensity (c) and frequency (d) of daily extremes. Forced changes are calculated as displayed in Figs. 1-4 and expressed as a percentage of the historical climatology (1850-1950). Hatching indicates grid-cells in which less than 80% (17/21) of the models agree on the sign of change.

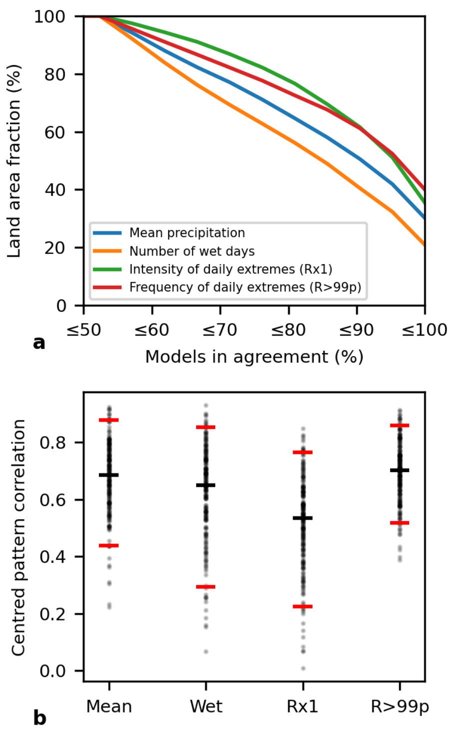

Fig. 6. The extent of inter-model agreement in the spatial pattern of forced precipitation change. (a) The land area on which models project the same sign of change as a function of the number of models in agreement. (b) Centred pattern correlations between the forced changes detected within individual CMIP6 models. Points show correlations between the 210 unique pairs of models, black and red lines show the median, 5^{th} and 95^{th} percentile of these correlations.

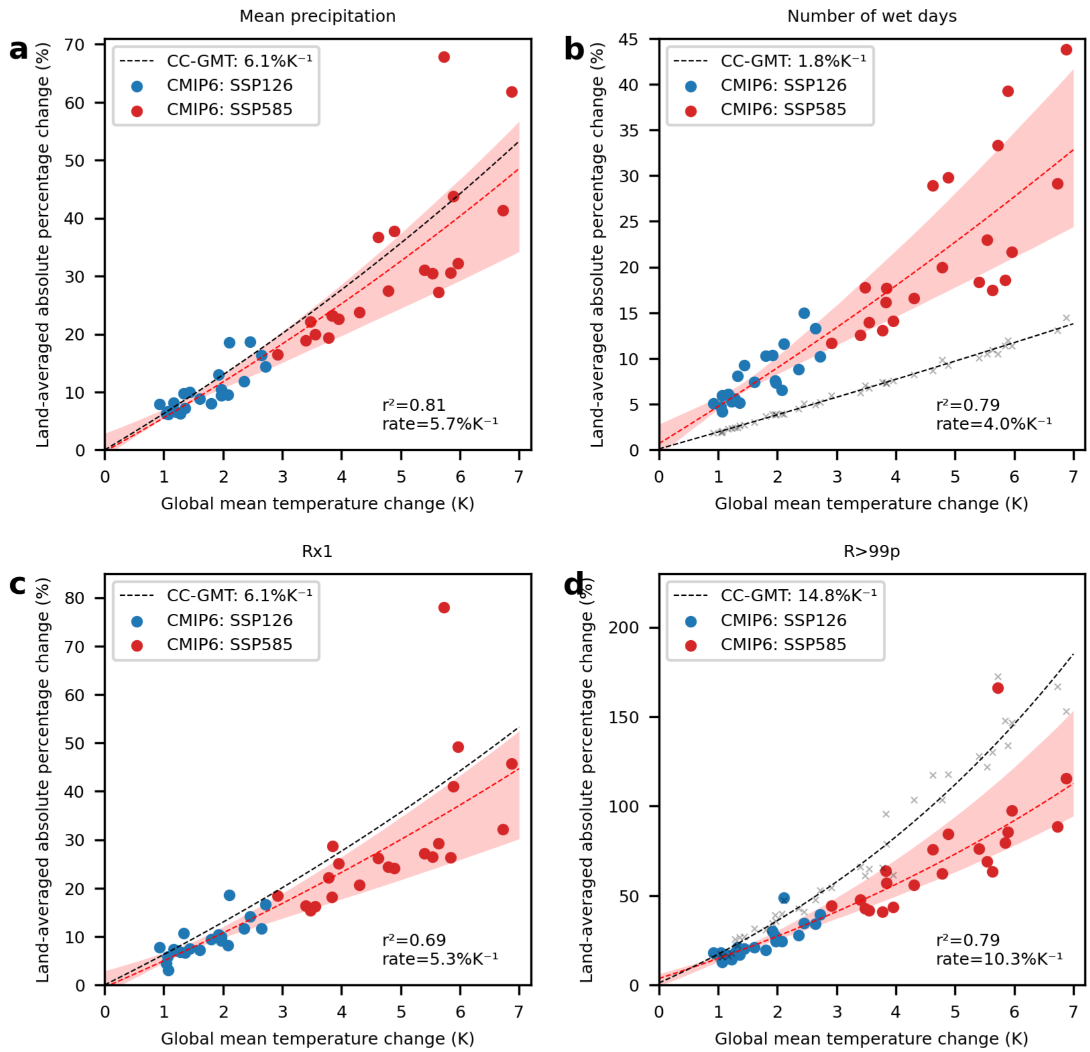

FIG. 7. The scaling of the average absolute local precipitation change with global mean temperature (GMT) across CMIP6 models and scenarios. Forced changes between 1950-1960 and 2090-2100 are calculated from the lowest-frequency component of each precipitation index (as in Figs. 1-4) and of annual mean temperature. Red and blue colors denote the SSP585 and SSP126 scenarios of future greenhouse forcing. Dashed lines show the expected response based on the theoretical Clausius-Clapeyron relation (in black) and the results of an exponential regression (in red). The statistics of the regression are displayed below and the 5^{th} and 95^{th} confidence intervals based on bootstrapped estimates of the regression (1000 climate model resamples with replacement) outlined in red. The Clausius-Clapeyron relation for the number of wet days and the frequency of daily extremes (R>99p) are estimated by scaling up each day of the historical precipitation distribution (1850-1950) by the given level of GMT change, and re-calculating each index, following Fischer and Knutti (2016). Individual estimates from this method are shown in grey, the black dashed-line showing the result of an exponential regression to these estimates. The scaling rate of these regressions are displayed in the figure legend.

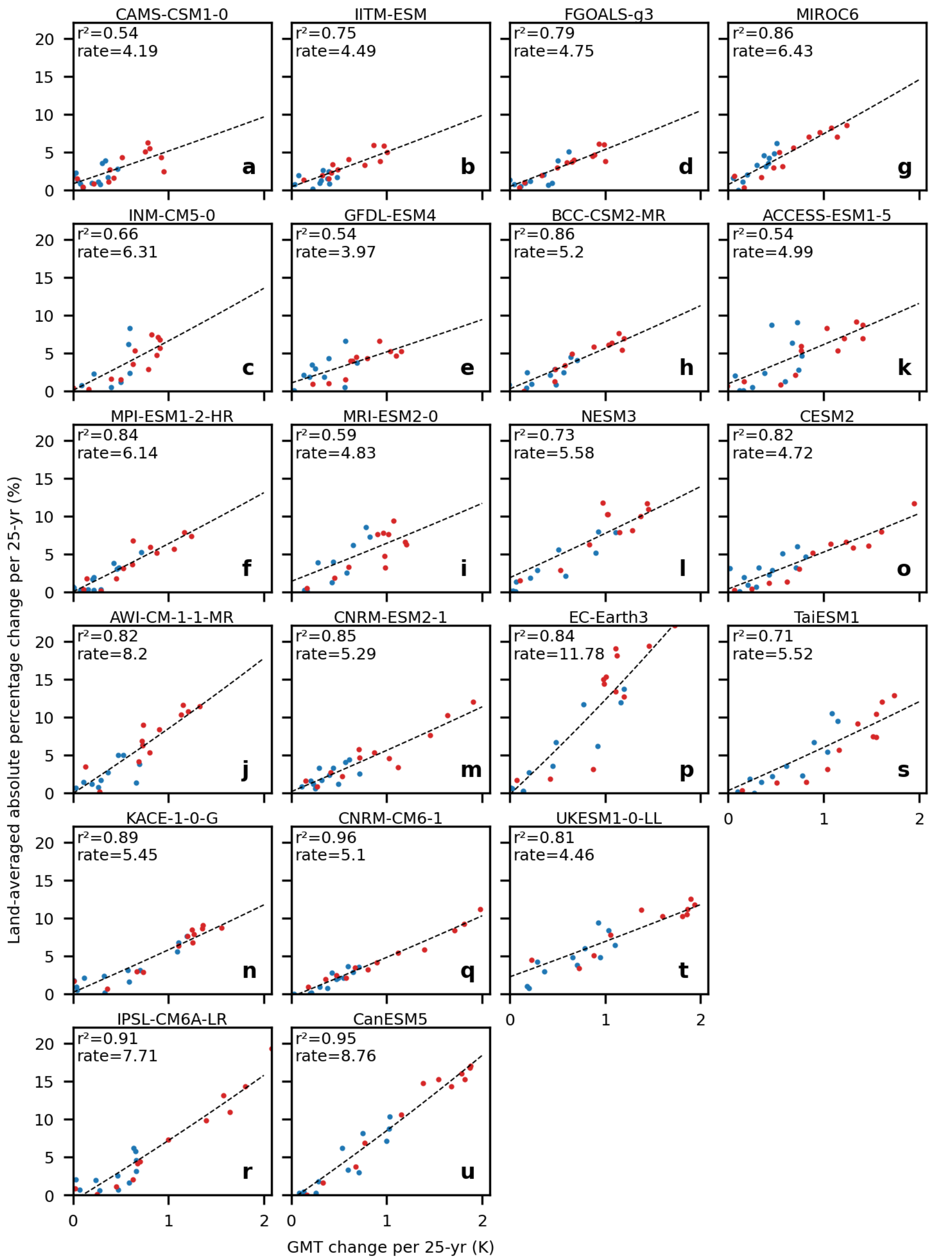

FIG. 8. The scaling of the average absolute local change of mean daily precipitation with global mean temperature (GMT) change within individual CMIP6 climate models, identified from changes between pairs of non-overlapping decades separated by 25 years. Forced changes are calculated from the lowest-frequency component detected with low-frequency component analysis. Red and blue colors denote the SSP585 and SSP126 scenarios of future greenhouse forcing and in black the results of a least-squares exponential regression are shown. Models are ordered (a-u, top-left to bottom-right) from lowest to highest GMT change as in Fig. 1.

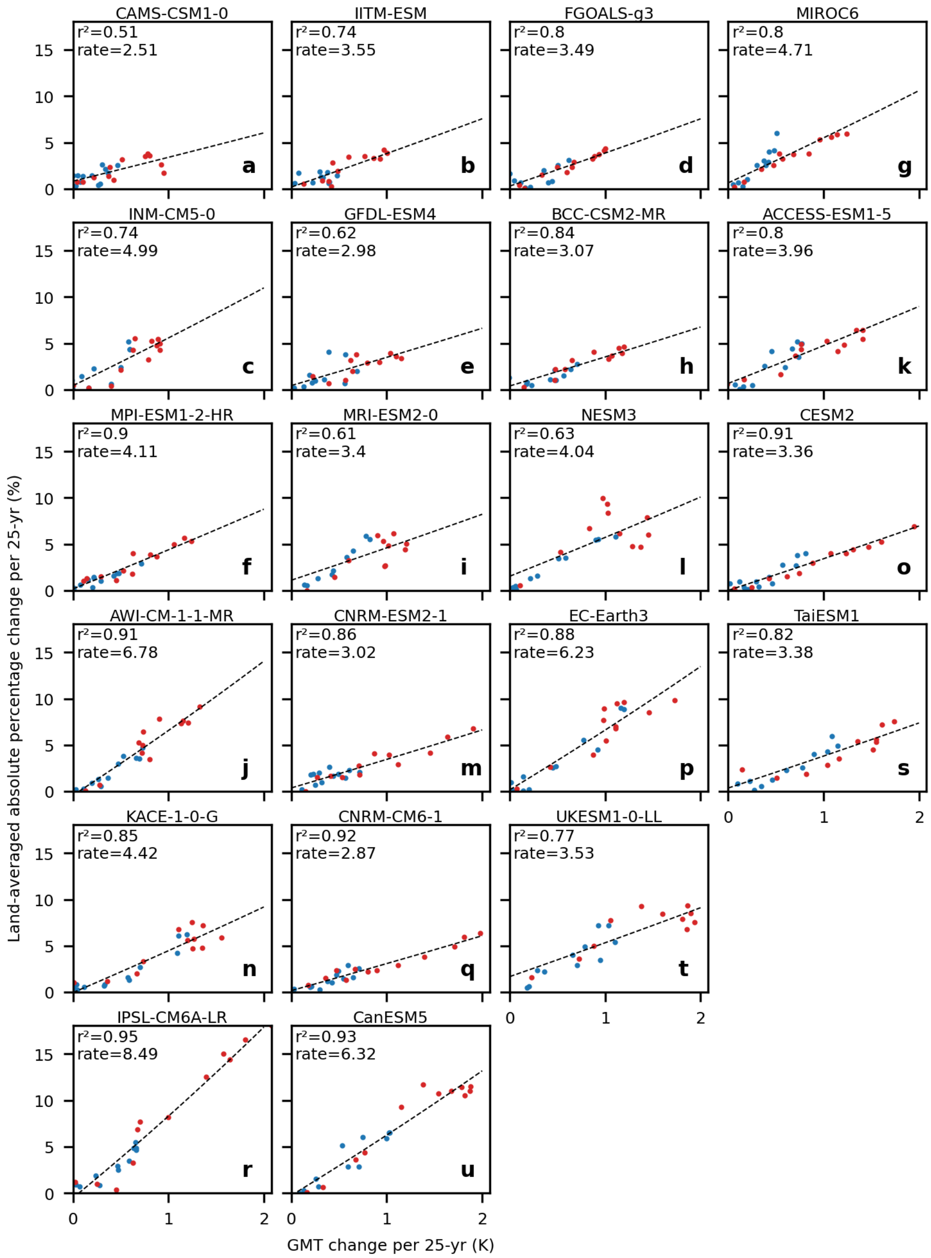

FIG. 9. As Fig. 8 but for changes in the number of wet days.

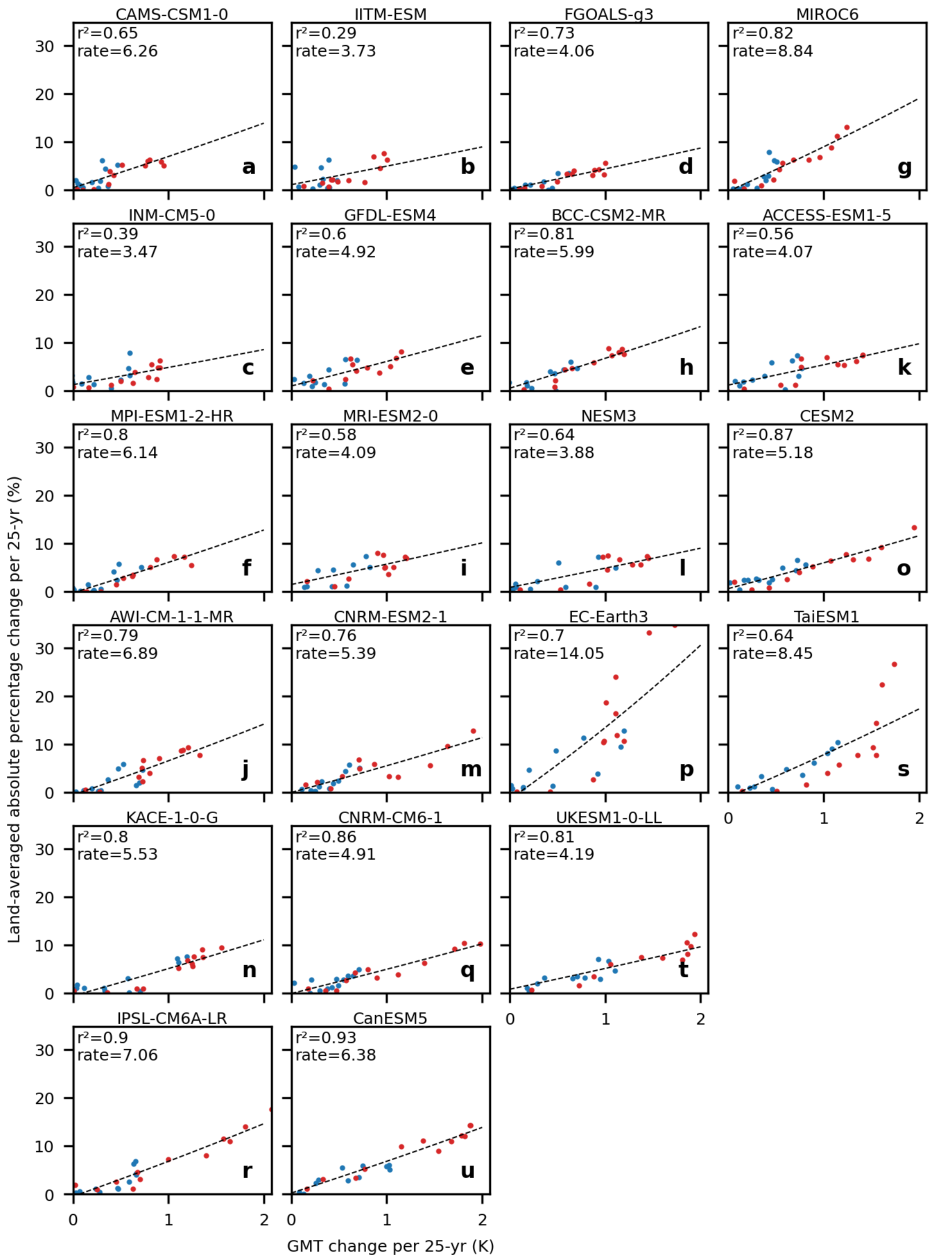

FIG. 10. As Fig. 8 but for changes in the intensity of daily extremes, measured as the annual maximum daily precipitation (Rx1).

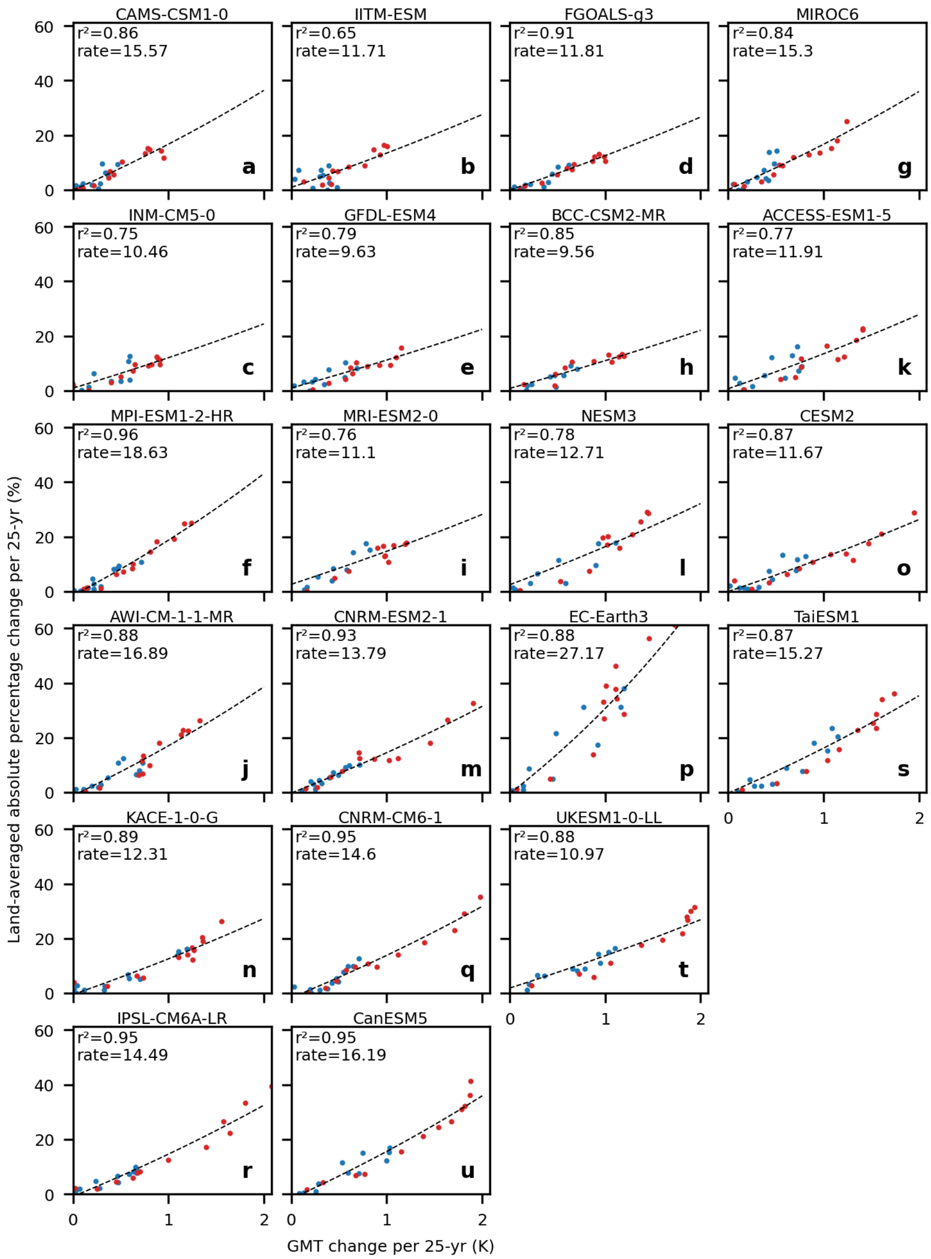

FIG. 11. As Fig. 8 but for changes in the frequency of daily extremes, measured as the annual number of days exceeding the 99^{th} percentile of the historical distribution (R>99).

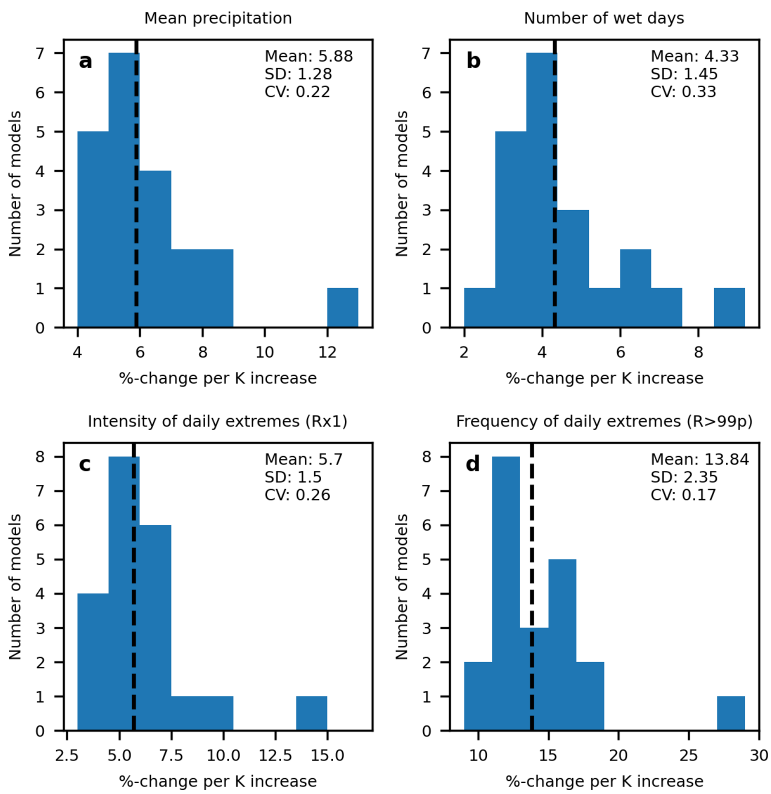

Fig. 12. Inter-model spread in the temperature-precipitation scaling relationships identified from the forced changes detected within individual CMIP6 models, for (a) mean precipitation, (b) the number of wet days and (c) the intensity (Rx1) and (d) frequency (R>99) of daily extremes. The mean, standard deviation, and coefficient of variation across models (excluding the prominent outlier 'EC-Earth3') are displayed with the mean denoted by the vertical dashed line.

Acknowledgments. MK and LW received funding from the Volkswagen foundation. SL received funding from the German Research Foundation (DFG, project number 427397136) and from the German Federal Ministry of Education and Research (BMBF, project number 01LP1907A). AL received funding from the Horizon 2020 Framework Programme of the European Union (grant agreement number 820712).

Data availability statement. Raw CMIP6 data is available from https://esgf-node.llnl.gov/projects/cmip6/. Bias-adjusted CMIP6 data is available for 10 models from the ISIMIP repository https://doi.org/10.48364/ISIMIP.842396.1 and https://doi.org/10.48364/ISIMIP.581124. Code for low-frequency component analysis is available from https://github.com/rcjwills/lfca. All other data and code is available form the authors upon request.

References

Bao, J., S. C. Sherwood, L. V. Alexander, and J. P. Evans, 2017: Future increases in extreme precipitation exceed observed scaling rates. *Nature Climate Change*, **7 (2)**, 128–132, https://doi.org/10.1038/nclimate3201, URL https://doi.org/10.1038/nclimate3201.

Bony, S., G. Bellon, D. Klocke, S. Sherwood, S. Fermepin, and S. Denvil, 2013: Robust direct effect of carbon dioxide on tropical circulation and regional precipitation. *Nature Geoscience*, **6 (6)**, 447–451, https://doi.org/10.1038/ngeo1799, URL https://doi.org/10.1038/ngeo1799.

Boulange, J., N. Hanasaki, D. Yamazaki, and Y. Pokhrel, 2021: Role of dams in reducing global flood exposure under climate change. *Nature Communications*, **12 (1)**, 417, https://doi.org/10.1038/s41467-020-20704-0, URL https://doi.org/10.1038/s41467-020-20704-0.

Ceppi, P., G. Zappa, T. G. Shepherd, and J. M. Gregory, 2018: Fast and slow components of the extratropical atmospheric circulation response to co2 forcing. *Journal of Climate*, **31 (3)**, 1091 – 1105, https://doi.org/10.1175/JCLI-D-17-0323.1, URL https://journals.ametsoc.org/view/journals/clim/31/3/jcli-d-17-0323.1.xml.

Chadwick, R., I. Boutle, and G. Martin, 2013: Spatial patterns of precipitation change in cmip5: Why the rich do not get richer in the tropics. *Journal of Climate*, **26 (11)**, 3803

– 3822, https://doi.org/10.1175/JCLI-D-12-00543.1, URL https://journals.ametsoc.org/view/journals/clim/26/11/jcli-d-12-00543.1.xml.

Chadwick, R., P. Good, T. Andrews, and G. Martin, 2014: Surface warming patterns drive tropical rainfall pattern responses to co2 forcing on all timescales. *Geophysical Research Letters*, **41 (2)**, 610–615, https://doi.org/https://doi.org/10.1002/2013GL058504, URL https://agupubs.onlinelibrary.wiley.com/doi/abs/10.1002/2013GL058504, https://agupubs.onlinelibrary.wiley.com/doi/pdf/10.1002/2013GL058504.

Chadwick, R., P. Good, G. Martin, and D. P. Rowell, 2016: Large rainfall changes consistently projected over substantial areas of tropical land. *Nature Climate Change*, **6 (2)**, 177–181, https://doi.org/10.1038/nclimate2805, URL https://doi.org/10.1038/nclimate2805.

Chen, H., and J. Sun, 2017: Contribution of human influence to increased daily precipitation extremes over china. *Geophysical Research Letters*, **44 (5)**, 2436–2444, https://doi.org/https://doi.org/10.1002/2016GL072439, URL https://agupubs.onlinelibrary.wiley.com/doi/abs/10.1002/2016GL072439, https://agupubs.onlinelibrary.wiley.com/doi/pdf/10.1002/2016GL072439.

Cucchi, M., G. P. Weedon, A. Amici, N. Bellouin, S. Lange, H. Müller Schmied, H. Hersbach, and C. Buontempo, 2020: Wfde5: bias-adjusted era5 reanalysis data for impact studies. *Earth System Science Data*, **12 (3)**, 2097–2120.

Damania, R., S. Desbureaux, and E. Zaveri, 2020: Does rainfall matter for economic growth? evidence from global sub-national data (1990–2014). *Journal of Environmental Economics and Management*, **102**, 102 335, https://doi.org/https://doi.org/10.1016/j.jeem.2020.102335, URL https://www.sciencedirect.com/science/article/pii/S0095069620300589.

Davenport, F. V., M. Burke, and N. S. Diffenbaugh, 2021: Contribution of historical precipitation change to us flood damages. *Proceedings of the National Academy of Sciences*, **118 (4)**, https://doi.org/10.1073/pnas.2017524118, URL https://www.pnas.org/content/118/4/e2017524118, https://www.pnas.org/content/118/4/e2017524118.full.pdf.

Deser, C., A. Phillips, V. Bourdette, and H. Teng, 2012: Uncertainty in climate change projections: the role of internal variability. *Climate Dynamics*, **38 (3)**, 527–546, https://doi.org/10.1007/s00382-010-0977-x, URL https://doi.org/10.1007/s00382-010-0977-x.

Deser, C., and A. S. Phillips, 2009: Atmospheric circulation trends, 1950–2000: The relative roles of sea surface temperature forcing and direct atmospheric radiative forcing. *Journal of Climate*, **22 (2)**, 396 – 413, https://doi.org/10.1175/2008JCLI2453.1, URL https://journals.ametsoc.org/view/journals/clim/22/2/2008jcli2453.1.xml.

Deser, C., A. S. Phillips, M. A. Alexander, and B. V. Smoliak, 2014: Projecting north american climate over the next 50 years: Uncertainty due to internal variability. *Journal of Climate*, **27 (6)**, 2271 – 2296, https://doi.org/10.1175/JCLI-D-13-00451.1, URL https://journals.ametsoc.org/view/journals/clim/27/6/jcli-d-13-00451.1.xml.

Emori, S., and S. J. Brown, 2005: Dynamic and thermodynamic changes in mean and extreme precipitation under changed climate. *Geophysical Research Letters*, **32 (17)**, https://doi.org/https://doi.org/10.1029/2005GL023272, URL https://agupubs.onlinelibrary.wiley.com/doi/abs/10.1029/2005GL023272, https://agupubs.onlinelibrary.wiley.com/doi/pdf/10.1029/2005GL023272.

Eyring, V., S. Bony, G. A. Meehl, C. A. Senior, B. Stevens, R. J. Stouffer, and K. E. Taylor, 2016: Overview of the coupled model intercomparison project phase 6 (cmip6) experimental design and organization. *Geoscientific Model Development*, **9 (5)**, 1937–1958, https://doi.org/10.5194/gmd-9-1937-2016, URL https://gmd.copernicus.org/articles/9/1937/2016/.

Fereday, D., R. Chadwick, J. Knight, and A. A. Scaife, 2018: Atmospheric dynamics is the largest source of uncertainty in future winter european rainfall. *Journal of Climate*, **31 (3)**, 963 – 977, https://doi.org/10.1175/JCLI-D-17-0048.1, URL https://journals.ametsoc.org/view/journals/clim/31/3/jcli-d-17-0048.1.xml.

Fischer, E. M., and R. Knutti, 2016: Observed heavy precipitation increase confirms theory and early models. *Nature Climate Change*, **6 (11)**, 986–991, https://doi.org/10.1038/nclimate3110, URL https://doi.org/10.1038/nclimate3110.

Holtermann, L., 2020: Precipitation anomalies, economic production, and the role of “first-nature” and “second-nature” geographies: A disaggregated analysis in high-income countries. *Global Environmental Change*, **65**, 102 167, https://doi.org/https://doi.org/10.1016/j.gloenvcha.2020.102167, URL https://www.sciencedirect.com/science/article/pii/S0959378020307500.

Hsiang, S. M., M. Burke, and E. Miguel, 2013: Quantifying the influence of climate on human conflict. *Science*, **341 (6151)**, 1235 367, https://doi.org/10.1126/science.1235367.

Kay, J. E., and Coauthors, 2015: The community earth system model (cesm) large ensemble project: A community resource for studying climate change in the presence of internal climate variability. *Bulletin of the American Meteorological Society*, **96 (8)**, 1333 – 1349, https://doi.org/10.1175/BAMS-D-13-00255.1, URL https://journals.ametsoc.org/view/journals/bams/96/8/bams-d-13-00255.1.xml.

Kent, C., R. Chadwick, and D. P. Rowell, 2015: Understanding uncertainties in future projections of seasonal tropical precipitation. *Journal of Climate*, **28 (11)**, 4390 – 4413, https://doi.org/10.1175/JCLI-D-14-00613.1, URL https://journals.ametsoc.org/view/journals/clim/28/11/jcli-d-14-00613.1.xml.

Kirchmeier-Young, M. C., and X. Zhang, 2020: Human influence has intensified extreme precipitation in north america. *Proceedings of the National Academy of Sciences*, **117 (24)**, 13 308–13 313, https://doi.org/10.1073/pnas.1921628117, URL https://www.pnas.org/content/117/24/13308, https://www.pnas.org/content/117/24/13308.full.pdf.

Kotz, M., A. Levermann, and L. Wenz, 2022: The effect of rainfall changes on economic production. *Nature*, https://doi.org/10.1038/s41586-021-04283-8.

Kotz, M., L. Wenz, and A. Levermann, 2021: Footprint of greenhouse forcing in daily temperature variability. *Proceedings of the National Academy of Sciences*, **118 (32)**, https://doi.org/10.1073/pnas.2103294118, URL https://www.pnas.org/content/118/32/e2103294118, https://www.pnas.org/content/118/32/e2103294118.full.pdf.

Lange, S., 2019: Trend-preserving bias adjustment and statistical downscaling with isimip3basd (v1.0). *Geoscientific Model Development*, **12 (7)**, 3055–3070, https://doi.org/10.5194/gmd-12-3055-2019, URL https://gmd.copernicus.org/articles/12/3055/2019/.

Lange, S., 2021: ISIMIP3BASDv2.5.0. https://doi.org/10.5281/zenodo.4686991, URL https://doi.org/10.5281/zenodo.4686991.

Lange, S., and Coauthors, 2020: Projecting exposure to extreme climate impact events across six event categories and three spatial scales. *Earth's Future*, **8 (12)**, e2020EF001 616, https://doi.org/

https://doi.org/10.1029/2020EF001616, URL https://agupubs.onlinelibrary.wiley.com/doi/abs/10.1029/2020EF001616, e2020EF001616 10.1029/2020EF001616, https://agupubs.onlinelibrary.wiley.com/doi/pdf/10.1029/2020EF001616.

Lange, S., and Coauthors, 2021: WFDE5 over land merged with ERA5 over the ocean (W5E5 v2.0). https://doi.org/10.48364/ISIMIP.342217, URL https://doi.org/10.48364/ISIMIP.342217.

Liang, X.-Z., and Coauthors, 2017: Determining climate effects on us total agricultural productivity. *Proceedings of the National Academy of Sciences*, **114 (12)**, E2285–E2292, https://doi.org/10.1073/pnas.1615922114, URL https://www.pnas.org/content/114/12/E2285, https://www.pnas.org/content/114/12/E2285.full.pdf.

Long, S.-M., S.-P. Xie, and W. Liu, 2016: Uncertainty in tropical rainfall projections: Atmospheric circulation effect and the ocean coupling. *Journal of Climate*, **29 (7)**, 2671 – 2687, https://doi.org/10.1175/JCLI-D-15-0601.1, URL https://journals.ametsoc.org/view/journals/clim/29/7/jcli-d-15-0601.1.xml.

Ma, J., and S.-P. Xie, 2013: Regional patterns of sea surface temperature change: A source of uncertainty in future projections of precipitation and atmospheric circulation. *Journal of Climate*, **26 (8)**, 2482 – 2501, https://doi.org/10.1175/JCLI-D-12-00283.1, URL https://journals.ametsoc.org/view/journals/clim/26/8/jcli-d-12-00283.1.xml.

Madakumbura, G., C. C.W. Thackeray, and J. J. Norris, 2021: Anthropogenic influence on extreme precipitation over global land areas seen in multiple observational datasets. *Nature Communications*, **12 (3944)**, https://doi.org/10.1073/pnas.1921628117.

Marvel, K., and C. Bonfils, 2013: Identifying external influences on global precipitation. *Proceedings of the National Academy of Sciences*, **110 (48)**, 19 301–19 306, https://doi.org/10.1073/pnas.1314382110, URL https://www.pnas.org/content/110/48/19301, https://www.pnas.org/content/110/48/19301.full.pdf.

Masson-Delmotte, V., and Coauthors, 2021: IPCC, 2021: Climate Change 2021: The Physical Science Basis. Contribution of Working Group I to the Sixth Assessment Report of the Intergovernmental Panel on Climate Change. *Cambridge University Press. In Press.*

Min, S.-K., X. Zhang, F. W. Zwiers, and G. C. Hegerl, 2011: Human contribution to more-intense precipitation extremes. *Nature*, **470 (7334)**, 378–381, https://doi.org/10.1038/nature09763, URL https://doi.org/10.1038/nature09763.

Myhre, G., and Coauthors, 2019: Frequency of extreme precipitation increases extensively with event rareness under global warming. *Scientific Reports*, **9 (1)**, 16 063, https://doi.org/10.1038/s41598-019-52277-4, URL https://doi.org/10.1038/s41598-019-52277-4.

Neelin, J. D., S. Sahany, S. N. Stechmann, and D. N. Bernstein, 2017: Global warming precipitation accumulation increases above the current-climate cutoff scale. *Proceedings of the National Academy of Sciences*, **114 (6)**, 1258–1263, https://doi.org/10.1073/pnas.1615333114, URL https://www.pnas.org/content/114/6/1258, https://www.pnas.org/content/114/6/1258.full.pdf.

O'Gorman, P. A., 2012: Sensitivity of tropical precipitation extremes to climate change. *Nature Geoscience*, **5 (10)**, 697–700, https://doi.org/10.1038/ngeo1568, URL https://doi.org/10.1038/ngeo1568.

Pfahl, S., P. A. O'Gorman, and E. M. Fischer, 2017: Understanding the regional pattern of projected future changes in extreme precipitation. *Nature Climate Change*, **7 (6)**, 423–427, https://doi.org/10.1038/nclimate3287, URL https://doi.org/10.1038/nclimate3287.

Santer, B. D., K. E. Taylor, T. M. L. Wigley, J. E. Penner, P. D. Jones, and U. Cubasch, 1995: Towards the detection and attribution of an anthropogenic effect on climate. *Climate Dynamics*, **12 (2)**, 77–100, https://doi.org/10.1007/BF00223722, URL https://doi.org/10.1007/BF00223722.

Seager, R., N. Naik, and G. A. Vecchi, 2010: Thermodynamic and dynamic mechanisms for large-scale changes in the hydrological cycle in response to global warming. *Journal of Climate*, **23 (17)**, 4651 – 4668, https://doi.org/10.1175/2010JCLI3655.1, URL https://journals.ametsoc.org/view/journals/clim/23/17/2010jcli3655.1.xml.

Shaw, T. A., and A. Voigt, 2015: Tug of war on summertime circulation between radiative forcing and sea surface warming. *Nature Geoscience*, **8 (7)**, 560–566, https://doi.org/10.1038/ngeo2449, URL https://doi.org/10.1038/ngeo2449.

Shepherd, T. G., 2014: Atmospheric circulation as a source of uncertainty in climate change projections. *Nature Geoscience*, **7 (10)**, 703–708, https://doi.org/10.1038/ngeo2253, URL https://doi.org/10.1038/ngeo2253.

Sherwood, S. C., and Coauthors, 2020: An assessment of earth's climate sensitivity using multiple lines of evidence. *Reviews of Geophysics*, **58 (4)**, e2019RG000 678, https://doi.org/https://doi.org/10.1029/2019RG000678, URL https://agupubs.onlinelibrary.wiley.com/doi/abs/10.1029/2019RG000678, e2019RG000678 2019RG000678, https://agupubs.onlinelibrary.wiley.com/doi/pdf/10.1029/2019RG000678.

Stephens, G. L., and T. D. Ellis, 2008: Controls of global-mean precipitation increases in global warming gcm experiments. *Journal of Climate*, **21 (23)**, 6141 – 6155, https://doi.org/10.1175/2008JCLI2144.1, URL https://journals.ametsoc.org/view/journals/clim/21/23/2008jcli2144.1.xml.

Thiery, W., and Coauthors, 2021: Intergenerational inequities in exposure to climate extremes. *Science*, **374 (6564)**, 158–160, https://doi.org/10.1126/science.abi7339.

Vecchi, G. A., and B. J. Soden, 2007: Global warming and the weakening of the tropical circulation. *Journal of Climate*, **20 (17)**, 4316 – 4340, https://doi.org/10.1175/JCLI4258.1, URL https://journals.ametsoc.org/view/journals/clim/20/17/jcli4258.1.xml.

von Uexkull, N., M. Croicu, H. Fjelde, and H. Buhaug, 2016: Civil conflict sensitivity to growing-season drought. *Proceedings of the National Academy of Sciences*, **113 (44)**, 12 391–12 396, https://doi.org/10.1073/pnas.1607542113, URL https://www.pnas.org/content/113/44/12391, https://www.pnas.org/content/113/44/12391.full.pdf.

Warszawski, L., K. Frieler, V. Huber, F. Piontek, O. Serdeczny, and J. Schewe, 2014: The inter-sectoral impact model intercomparison project (isi–mip): Project framework. *Proceedings of the National Academy of Sciences*, **111 (9)**, 3228–3232, https://doi.org/10.1073/pnas.1312330110, URL https://www.pnas.org/content/111/9/3228, https://www.pnas.org/content/111/9/3228.full.pdf.

Willner, S. N., A. Levermann, F. Zhao, and K. Frieler, 2018a: Adaptation required to preserve future high-end river flood risk at present levels. *Science Advances*, **4 (1)**, eaao1914, https://doi.org/10.1126/sciadv.aao1914.

Willner, S. N., C. Otto, and A. Levermann, 2018b: Global economic response to river floods. *Nature Climate Change*, **8 (7)**, 594–598, https://doi.org/10.1038/s41558-018-0173-2, URL https://doi.org/10.1038/s41558-018-0173-2.

Wills, R. C., T. Schneider, J. M. Wallace, D. S. Battisti, and D. L. Hartmann, 2018: Disentangling global warming, multidecadal variability, and el niño in pacific temperatures. *Geophysical Research Letters*, **45 (5)**, 2487–2496, https://doi.org/https://doi.org/10.1002/2017GL076327, URL https://agupubs.onlinelibrary.wiley.com/doi/abs/10.1002/2017GL076327, https://agupubs.onlinelibrary.wiley.com/doi/pdf/10.1002/2017GL076327.

Wills, R. C. J., D. S. Battisti, K. C. Armour, T. Schneider, and C. Deser, 2020: Pattern recognition methods to separate forced responses from internal variability in climate model ensembles and observations. *Journal of Climate*, **33 (20)**, 8693 – 8719, https://doi.org/10.1175/JCLI-D-19-0855.1, URL https://journals.ametsoc.org/view/journals/clim/33/20/jcliD190855.xml.

Zhang, X., H. Wan, F. W. Zwiers, G. C. Hegerl, and S.-K. Min, 2013: Attributing intensification of precipitation extremes to human influence. *Geophysical Research Letters*, **40 (19)**, 5252–5257, https://doi.org/https://doi.org/10.1002/grl.51010, URL https://agupubs.onlinelibrary.wiley.com/doi/abs/10.1002/grl.51010, https://agupubs.onlinelibrary.wiley.com/doi/pdf/10.1002/grl.51010.

APPENDIX A

Forced response under SSP126

APPENDIX B

Spatial pattern of forced change

APPENDIX C

Inter-model temperature-precipitation scaling

APPENDIX D

Intra-model temperature-precipitation scaling

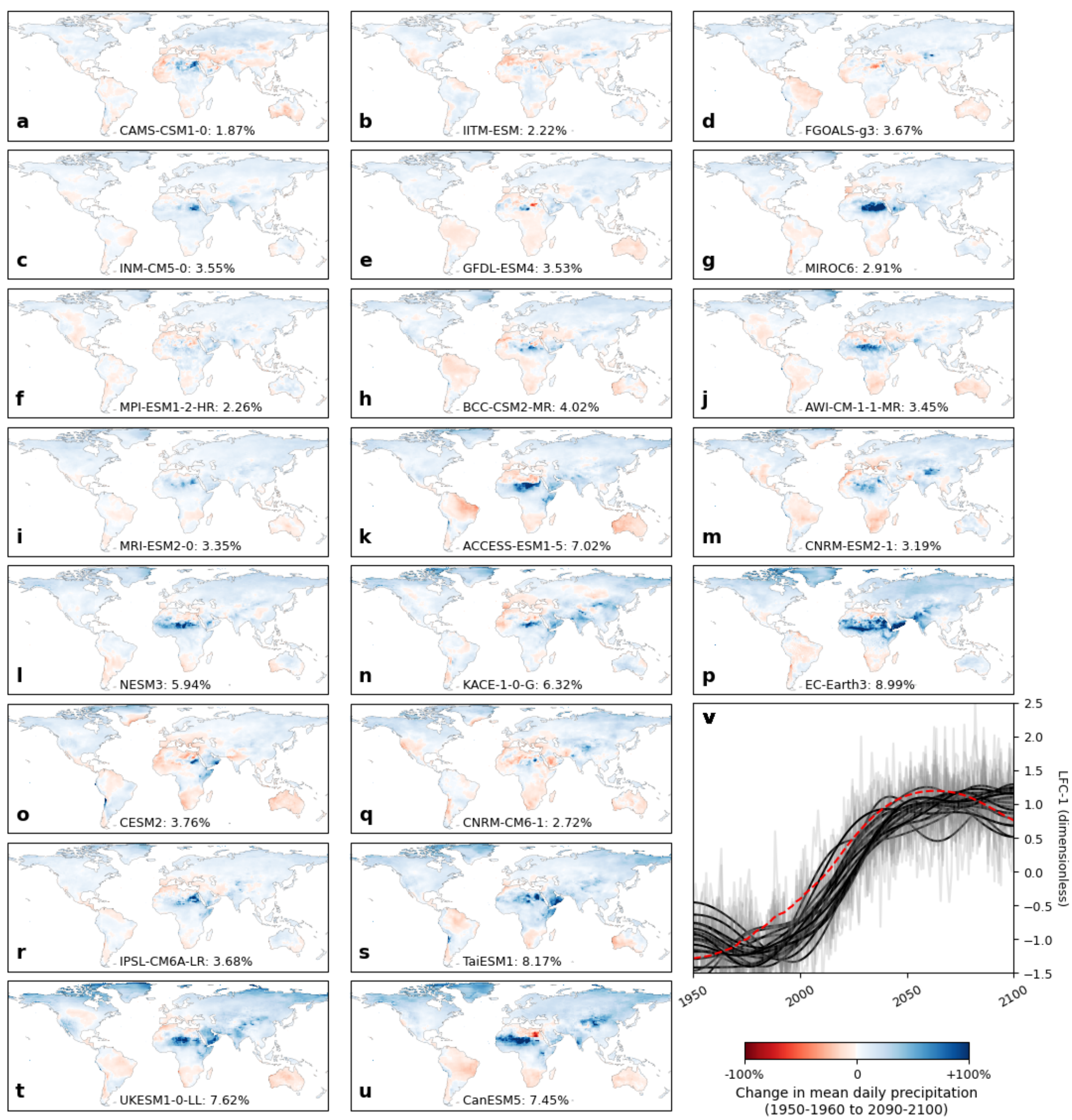

591 Fig. D1. The detected forced response of mean precipitation under historical and SSP126 scenario greenhouse
592 forcing. As Fig. 1 but for SSP126.

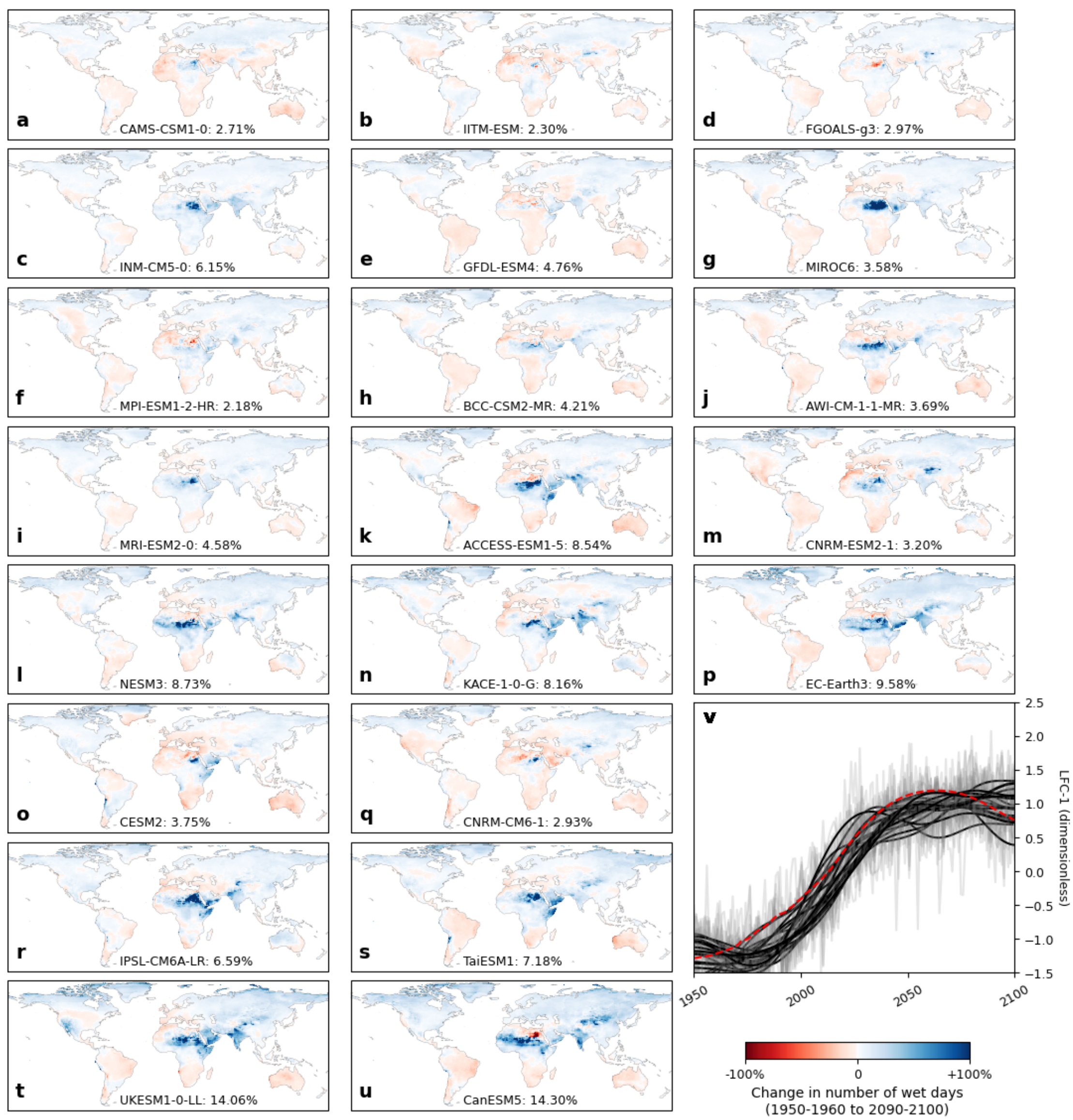

593 FIG. D2. The detected forced response of the number of wet days under historical and SSP126 scenario greenhouse forcing. As Fig. 2 but for SSP126.

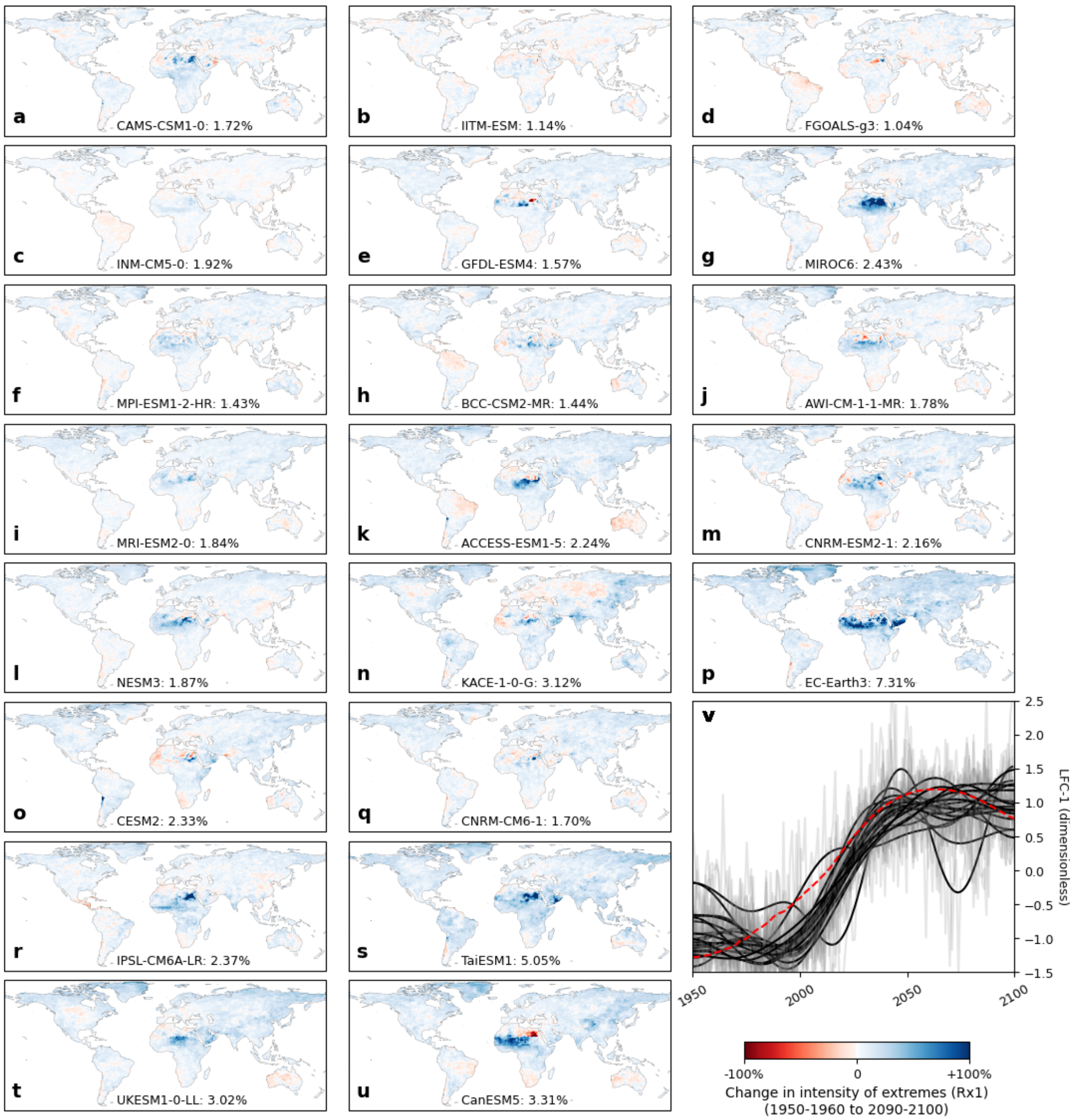

FIG. D3. The detected forced response of the intensity of daily precipitation extremes (Rx1) under historical and SSP126 scenario greenhouse forcing. As Fig. 3 but for SSP126.

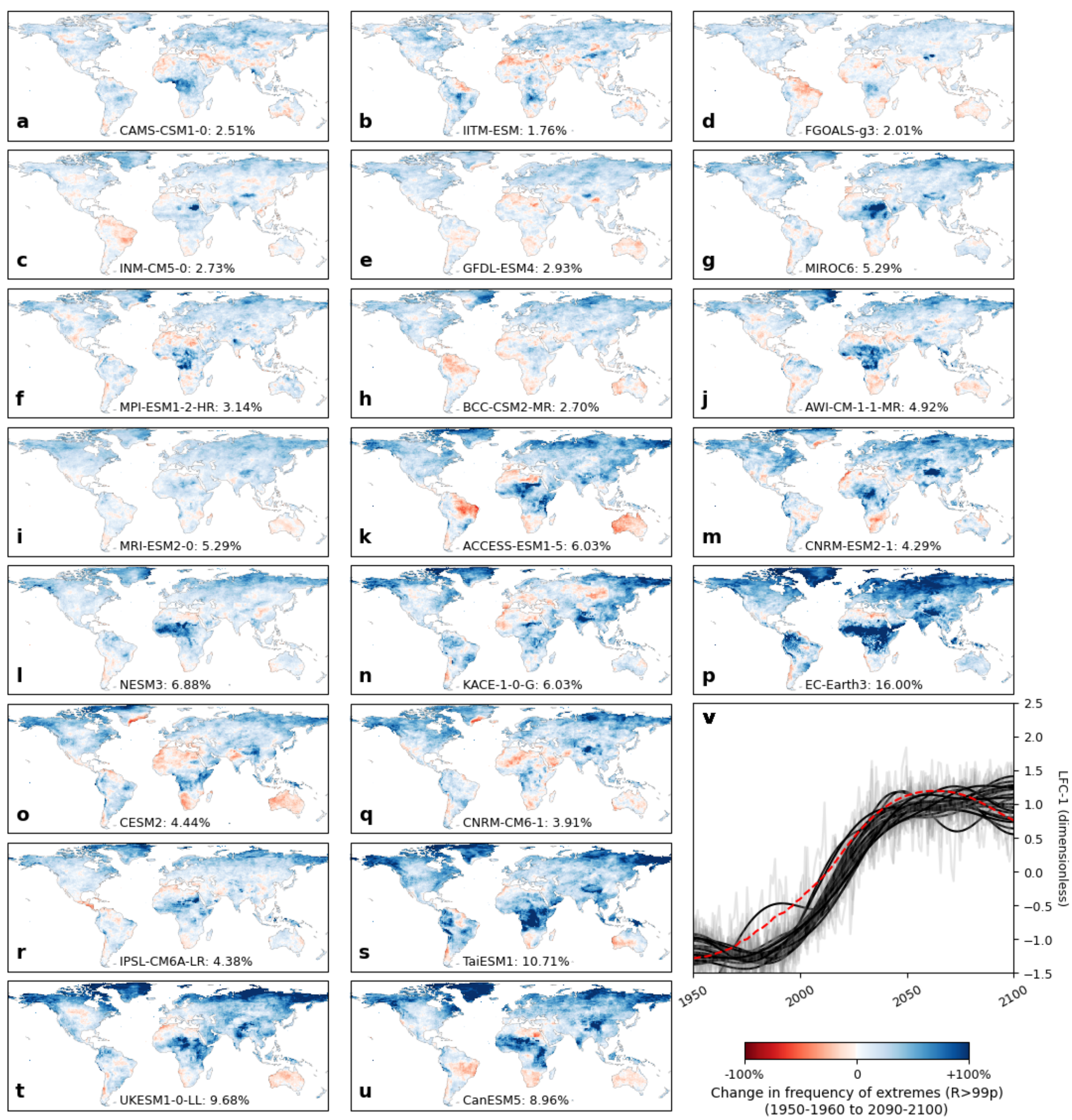

597 Fig. D4. The detected forced response of the frequency of daily precipitation extremes (R>99p) under historical
598 and SSP126 scenario greenhouse forcing. As Fig. 4 but for SSP126.

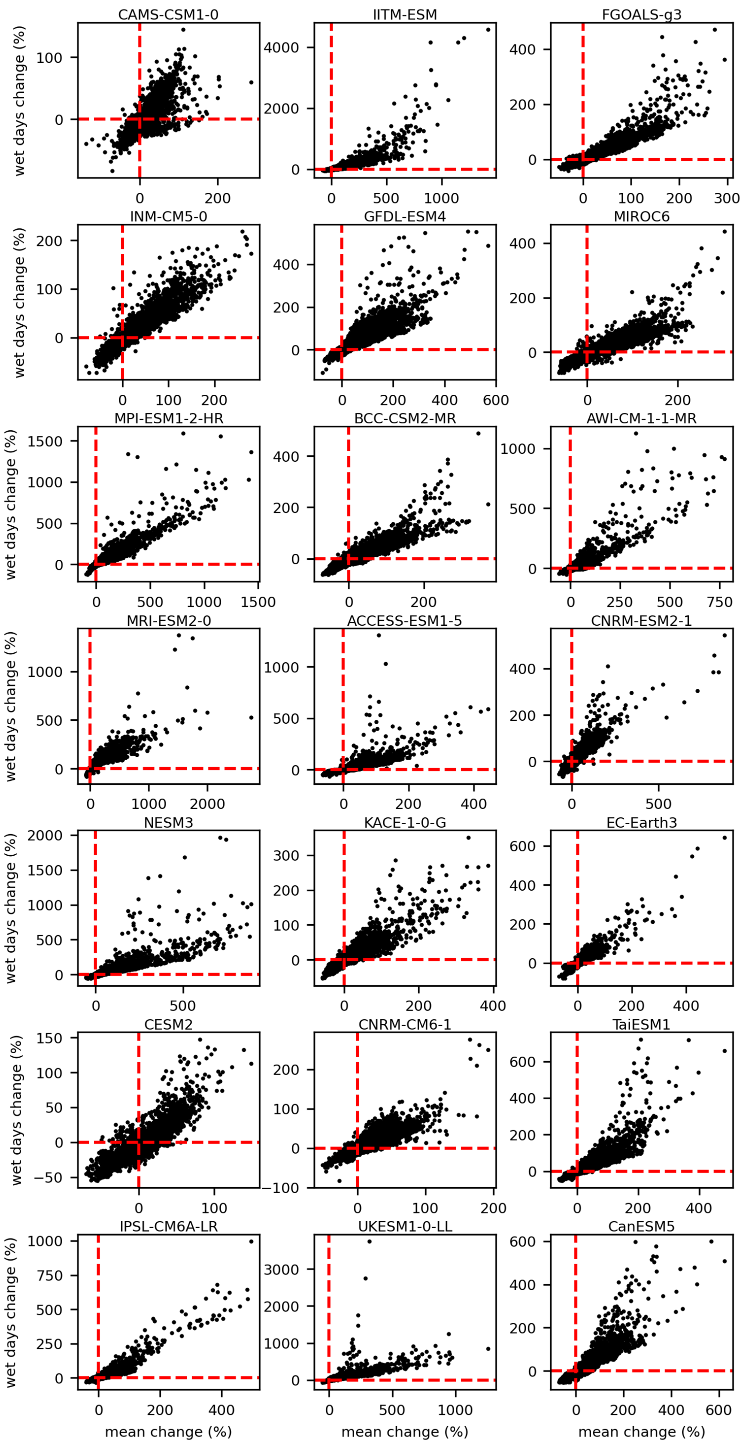

FIG. D5. Scatter plots between grid-cell forced changes in mean precipitation and the number of wet days for different members of the CMIP6 ensemble. Forced changes are calculated from the lowest-frequency component detected with low-frequency component analysis as in Fig. 1.

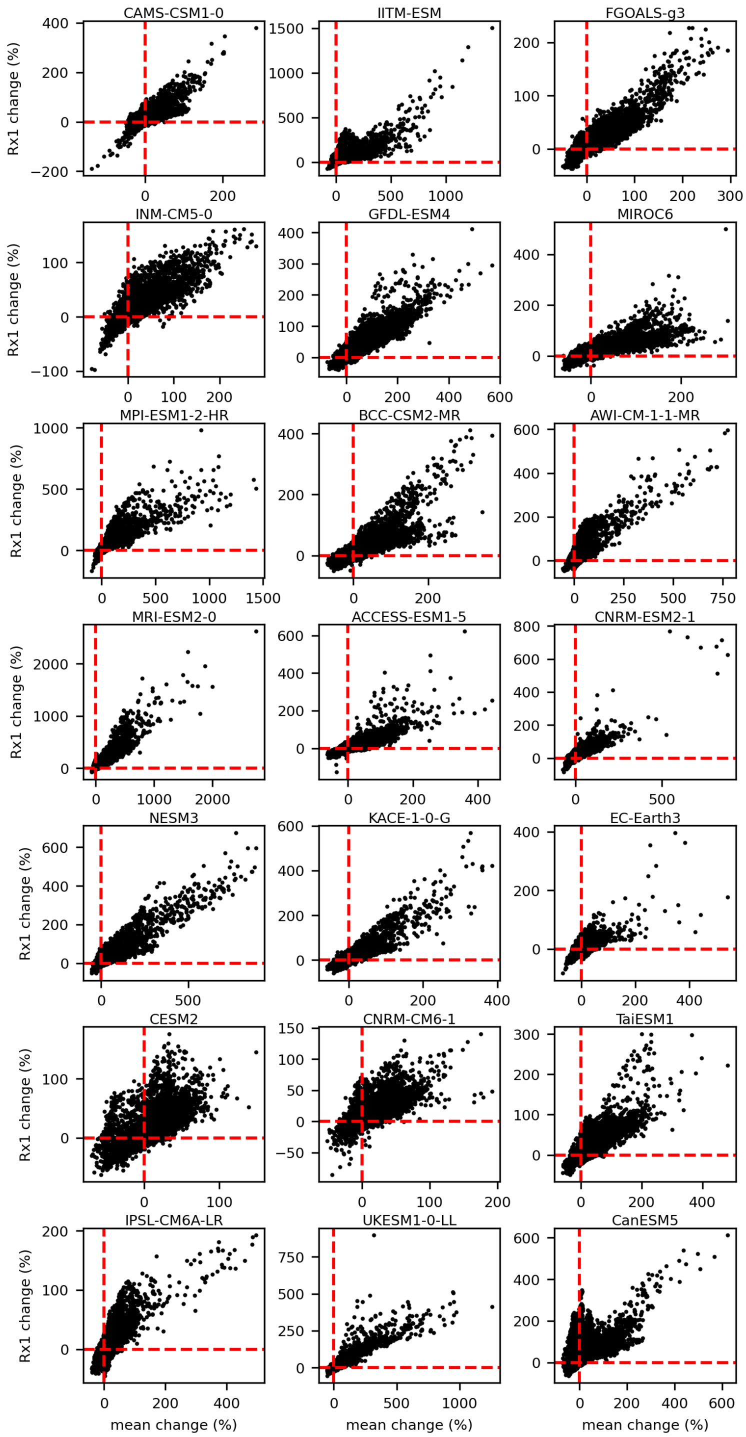

FIG. D6. Scatter plots between grid-cell forced changes in mean precipitation and the intensity of daily precipitation extremes (Rx1) for different members of the CMIP6 ensemble. Forced changes are calculated from the lowest-frequency component detected with low-frequency component analysis as in Fig. 1.

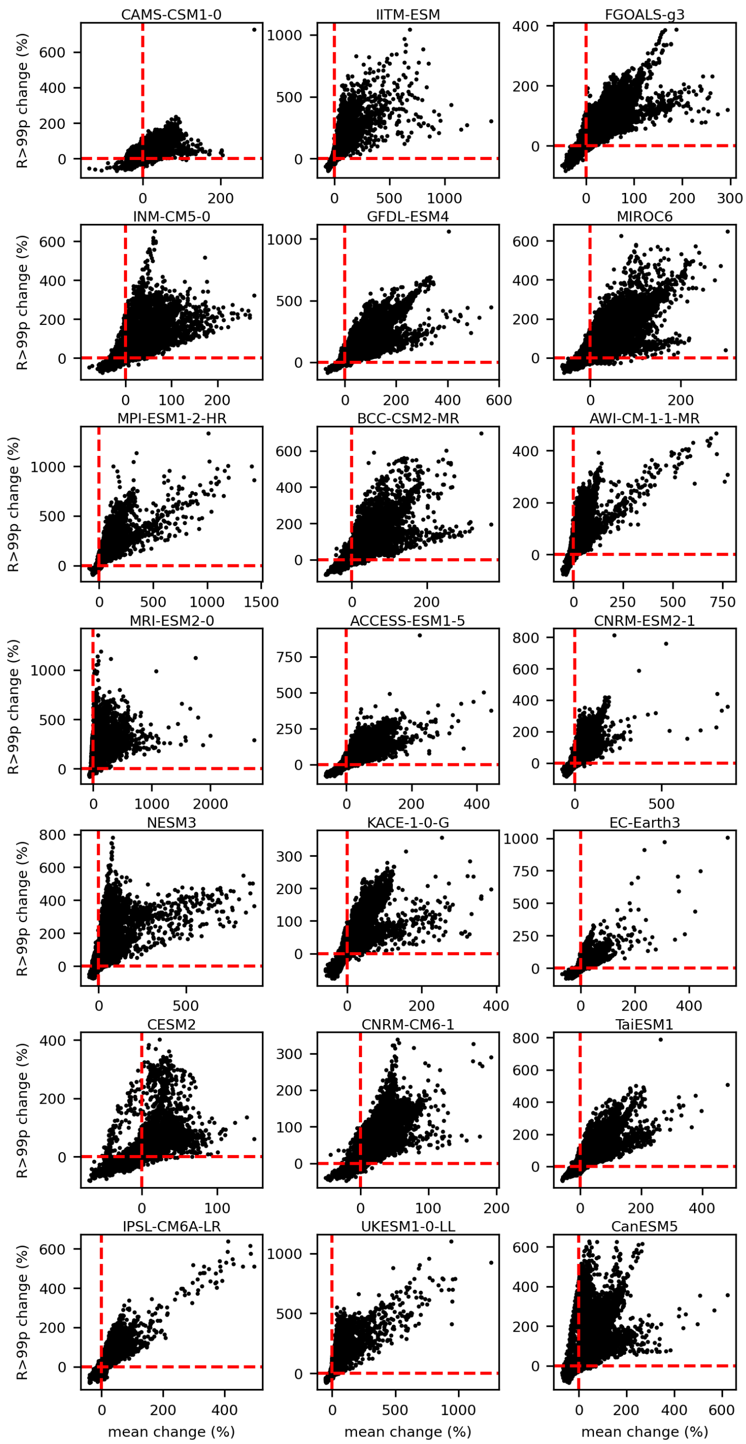

Fig. D7. Scatter plots between grid-cell forced changes in mean precipitation and the frequency of daily precipitation extremes (R>99p) for different members of the CMIP6 ensemble. Forced changes are calculated from the lowest-frequency component detected with low-frequency component analysis as in Fig. 1.

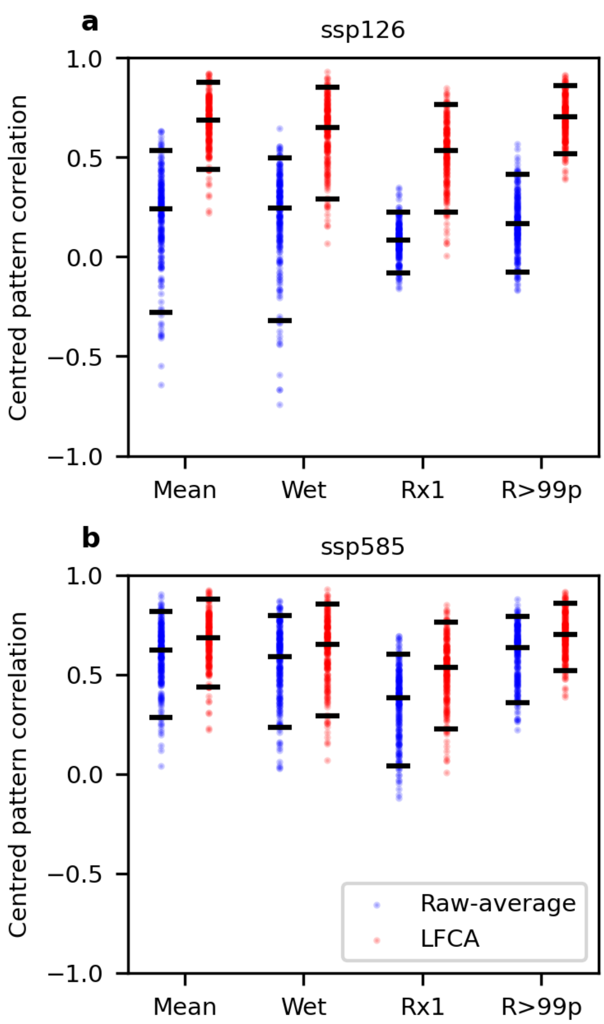

Fig. D8. Inter-model agreement in the spatial pattern of forced precipitation change when detected with either decadal averages or low-frequency component analysis (LFCA). Inter-model pattern correlations are calculated between the 210 unique pairs of models for forced changes in mean precipitation, the number of wet days and the intensity (Rx1) and frequency (R>99p) of daily extremes. Forced changes (1950-60 to 2090-2100) are calculated as the difference between either decadal averages of the raw data, or of the lowest-frequency component identified with LFCA, expressed as percentage changes of the historical climatology 1850-1950. The median and 5^{th} and 95^{th} percentiles of these pattern correlations are displaced as horizontal lines.

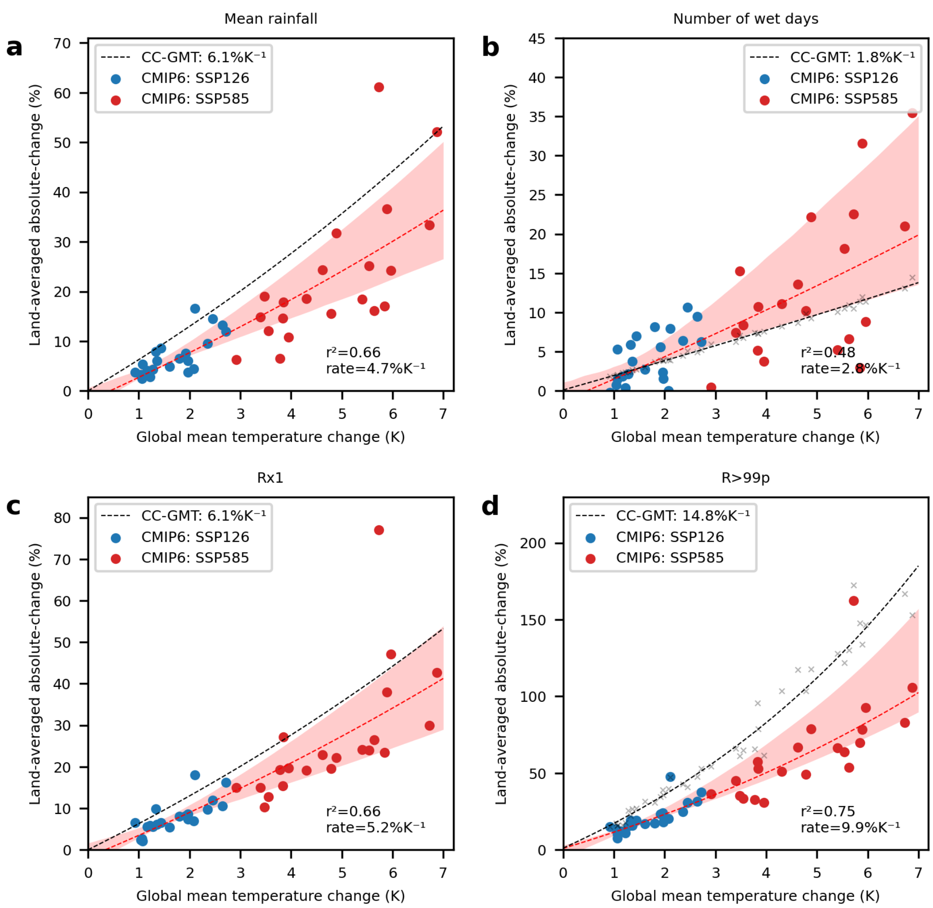

FIG. D9. Scaling between precipitation changes and GMT change without taking absolute values. As Fig. 7 but without taking absolute values of regional precipitation change.

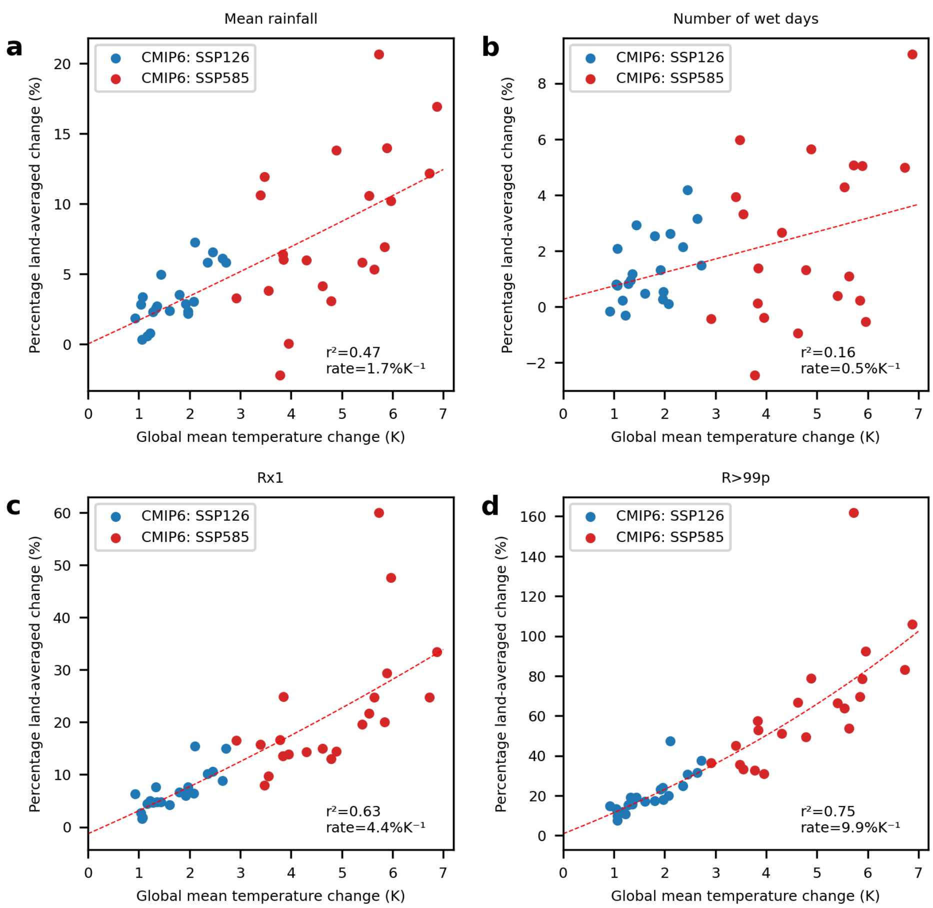

617 FIG. D10. Scaling between net precipitation changes and GMT change. As Fig. 7 but without taking absolute
618 values and taking percentages at the global, rather than local, level.

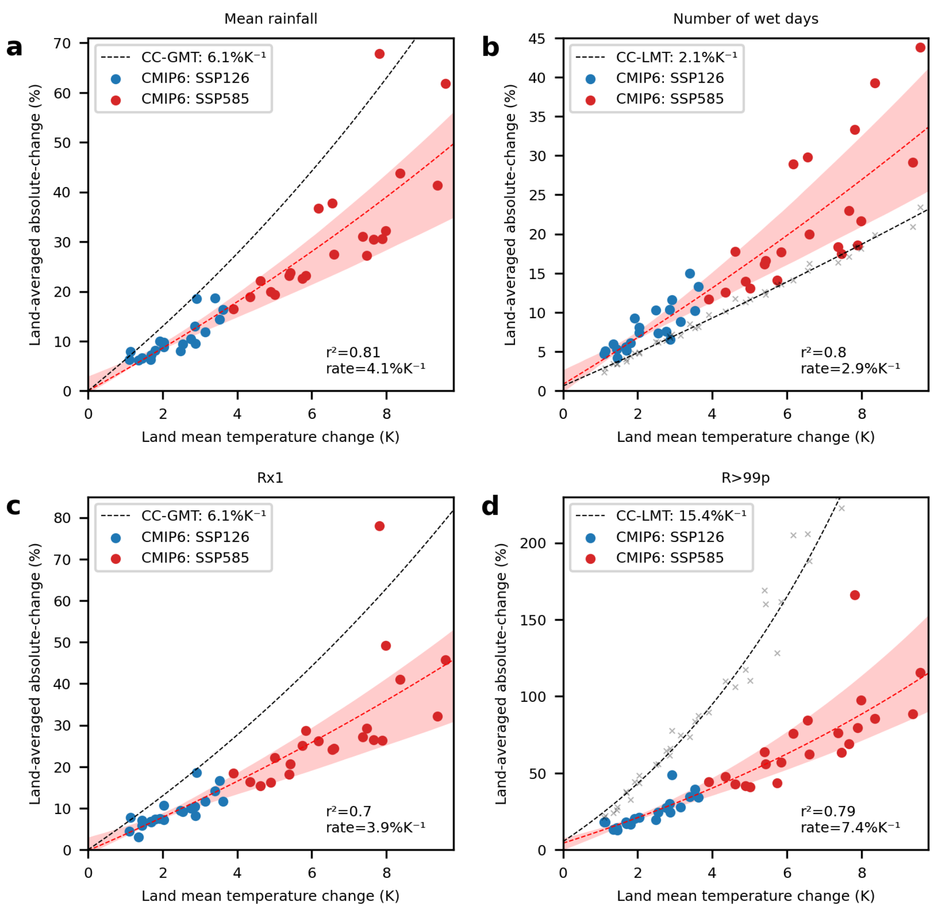

619 FIG. D11. Scaling between precipitation changes and land mean temperature change. As Fig. 7 but using land
620 rather than global mean temperature change.

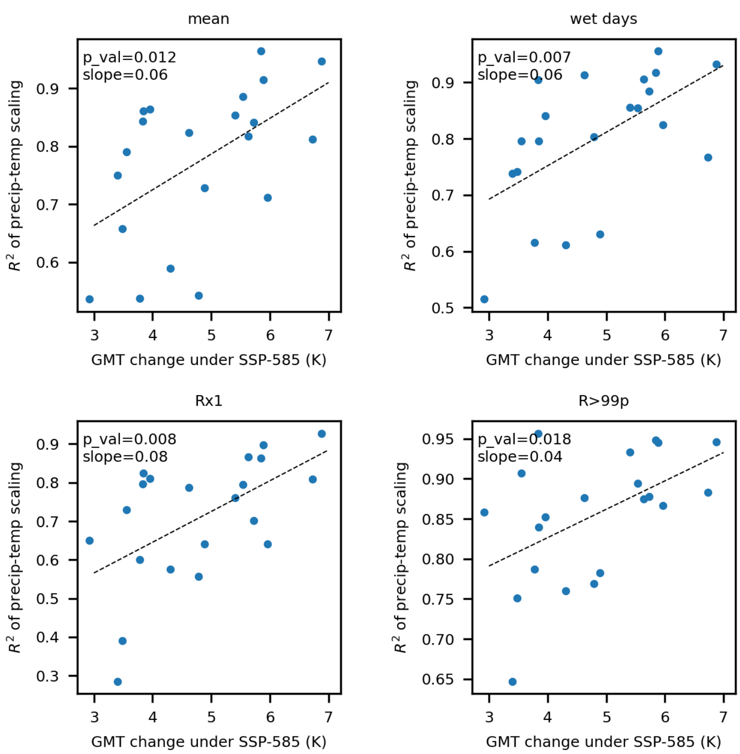

621 Fig. D12. Inter-model relationship between the R^2 of the intra-model precipitation-temperature scaling
622 relationship and the extent of GMT change.

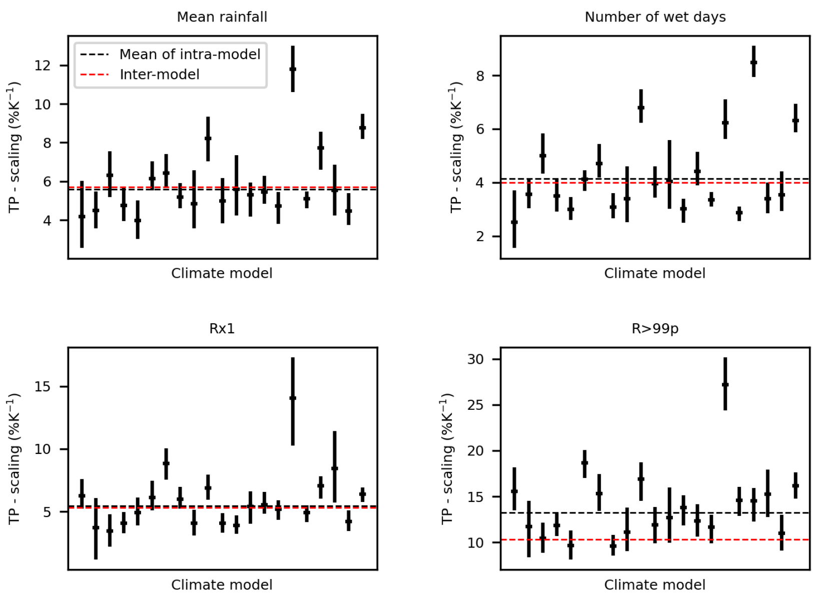

623 FIG. D13. Assessing the significance of inter-model differences in the intra-model temperature-precipitation scaling rate. A distribution of intra-model temperature-precipitation scaling rates are estimated for each model using boostrapped estimates of the regressions shown in Figs. 8-11 with 1000 replacements of inter-temporal changes. These distributions are shown with the central estimate for each climate model for forced changes in mean precipitation, the number of wet days and the intensity (Rx1) and frequency (R>99p) of daily precipitation. The mean intra-model scaling and the inter-model scaling (identified in Fig. 7) are shown as dashed horizontal lines in black and red respectively. Using these uncertainty distributions of the scaling rate of each model, we calculate that inter-model differences in the scaling rate are significantly non-zero at the 10% level for 47, 60, 58 and 64% of unique model pairs for mean precipitation, the number of wet days, Rx1 and R>99p respectively.

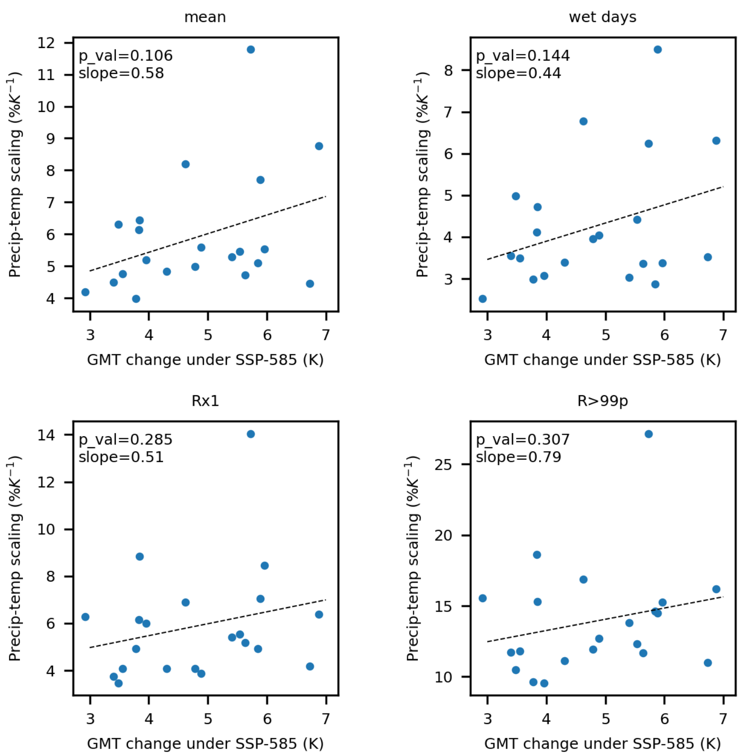

632 FIG. D14. Inter-model relationship between the intra-model rate of precipitation-temperature scaling and the
633 extent of GMT change.

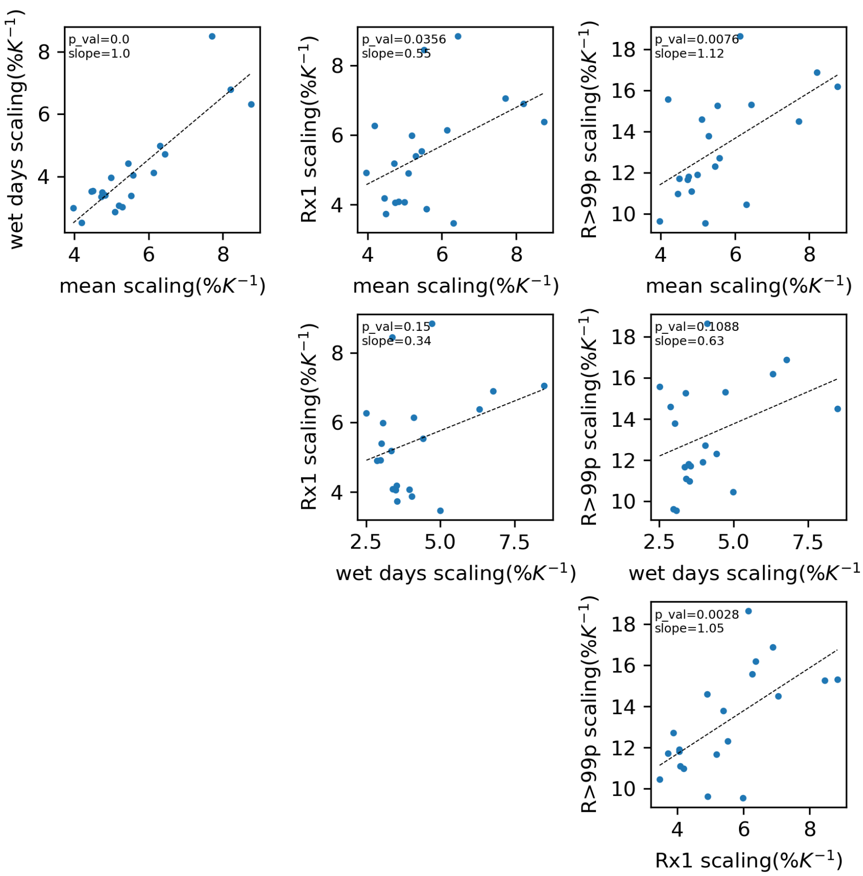

FIG. D15. Inter-model relationship between the intra-model rates of precipitation-temperature scaling for different precipitation indices, having removed the prominent outlier 'EC-Earth3'.